

Properties of slowly rotating asteroids from the Convex Inversion Thermophysical Model

A. Marciniak, J. Ďurech, V. Alí-Lagoa, W. Ogloza, R. Szakáts, T. G. Müller, L. Molnár, A. Pál, F. Monteiro, P. Arcoverde, et al.

▶ **To cite this version:**

A. Marciniak, J. Ďurech, V. Alí-Lagoa, W. Ogloza, R. Szakáts, et al.. Properties of slowly rotating asteroids from the Convex Inversion Thermophysical Model. Astronomy and Astrophysics - A&A, 2021, 654, 10.1051/0004-6361/202140991 . insu-03667381

HAL Id: insu-03667381
https://insu.hal.science/insu-03667381

Submitted on 13 May 2022

HAL is a multi-disciplinary open access archive for the deposit and dissemination of scientific research documents, whether they are published or not. The documents may come from teaching and research institutions in France or abroad, or from public or private research centers.

L'archive ouverte pluridisciplinaire **HAL**, est destinée au dépôt et à la diffusion de documents scientifiques de niveau recherche, publiés ou non, émanant des établissements d'enseignement et de recherche français ou étrangers, des laboratoires publics ou privés.

A&A 654, A87 (2021)
https://doi.org/10.1051/0004-6361/202140991
© ESO 2021

Astronomy & Astrophysics

Properties of slowly rotating asteroids from the Convex Inversion Thermophysical Model*

A. Marciniak[1], J. Ďurech[2], V. Alí-Lagoa[3], W. Ogłoza[4], R. Szakáts[5], T. G. Müller[3], L. Molnár[5,6,7], A. Pál[5,8], F. Monteiro[9], P. Arcoverde[9], R. Behrend[10], Z. Benkhaldoun[11], L. Bernasconi[12], J. Bosch[13], S. Brincat[14], L. Brunetto[15], M. Butkiewicz - Bąk[1], F. Del Freo[16], R. Duffard[17], M. Evangelista-Santana[9], G. Farroni[18], S. Fauvaud[19,20], M. Fauvaud[19,20], M. Ferrais[21], S. Geier[22,23], J. Golonka[24], J. Grice[25], R. Hirsch[1], J. Horbowicz[1], E. Jehin[26], P. Julien[14], Cs. Kalup[5], K. Kamiński[1], M. K. Kamińska[1], P. Kankiewicz[27], V. Kecskeméthy[5], D.-H. Kim[28,29], M.-J. Kim[29], I. Konstanciak[1], J. Krajewski[1], V. Kudak[30,31], P. Kulczak[1], T. Kundera[4], D. Lazzaro[9], F. Manzini[15], H. Medeiros[9,22], J. Michimani-Garcia[9], N. Morales[17], J. Nadolny[22,32], D. Oszkiewicz[1], E. Pakštienė[33], M. Pawłowski[1], V. Perig[31], F. Pilcher[34], P. Pinel[†,18], E. Podlewska-Gaca[1], T. Polakis[35], F. Richard[20], T. Rodrigues[9], E. Rondón[9], R. Roy[36], J. J. Sanabria[22], T. Santana-Ros[37,38], B. Skiff[39], J. Skrzypek[1], K. Sobkowiak[1], E. Sonbas[40], G. Stachowski[4], J. Strajnic[16], P. Trela[1], Ł. Tychoniec[41], S. Urakawa[42], E. Verebelyi[5], K. Wagrez[16], M. Żejmo[43], and K. Żukowski[1]

(Affiliations can be found after the references)

Received 2 April 2021 / Accepted 20 June 2021

ABSTRACT

Context. Recent results for asteroid rotation periods from the TESS mission showed how strongly previous studies have underestimated the number of slow rotators, revealing the importance of studying those targets. For most slowly rotating asteroids (those with $P > 12$ h), no spin and shape model is available because of observation selection effects. This hampers determination of their thermal parameters and accurate sizes. Also, it is still unclear whether signatures of different surface material properties can be seen in thermal inertia determined from mid-infrared thermal flux fitting.

Aims. We continue our campaign in minimising selection effects among main belt asteroids. Our targets are slow rotators with low light-curve amplitudes. Our goal is to provide their scaled spin and shape models together with thermal inertia, albedo, and surface roughness to complete the statistics.

Methods. Rich multi-apparition datasets of dense light curves are supplemented with data from *Kepler* and TESS spacecrafts. In addition to data in the visible range, we also use thermal data from infrared space observatories (mainly IRAS, Akari and WISE) in a combined optimisation process using the Convex Inversion Thermophysical Model. This novel method has so far been applied to only a few targets, and therefore in this work we further validate the method itself.

Results. We present the models of 16 slow rotators, including two updated models. All provide good fits to both thermal and visible data. The obtained sizes are on average accurate at the 5% precision level, with diameters found to be in the range from 25 to 145 km. The rotation periods of our targets range from 11 to 59 h, and the thermal inertia covers a wide range of values, from 2 to <400 J m^{-2} s$^{-1/2}$ K^{-1}, not showing any correlation with the period.

Conclusions. With this work we increase the sample of slow rotators with reliable spin and shape models and known thermal inertia by 40%. The thermal inertia values of our sample do not display a previously suggested increasing trend with rotation period, which might be due to their small skin depth.

Key words. minor planets, asteroids: general – techniques: photometric – radiation mechanisms: thermal

1. Introduction

Physical parameters of asteroids, such as spin, shape, size, albedo, macroscopic roughness, and thermal inertia, form the basis for a significant number of Solar System studies. In particular, these parameters are of great interest for large asteroids as these are considered remnants of early phases of planetary formation (Morbidelli et al. 2009). Studying the way in which asteroid surfaces react to heating by the Sun (which, among others, depends on the spin axis inclination and spin rate), can reveal material properties of these layers (Murdoch et al. 2015; Keihm et al. 2012). Slowly rotating asteroids, with periods longer than 12 h, are especially interesting in this respect; they experience long periods of irradiation of the same surface parts, and the diurnal heat wave from solar irradiation can penetrate to larger thermal skin depths (Delbo' et al. 2015; Čapek & Vokrouhlický 2010). Furthermore, the most recent results from the TESS mission (Transiting Exoplanet Survey Satellite; Ricker et al. 2015) reveal that slow rotators actually dominate the population of main-belt asteroids (see Fig. 7 in Pál et al. 2020). So far, however, they have been largely omitted by most ground-based studies mainly because of telescope time limitations and the small number of targeted campaigns (Warner & Harris 2011).

* The photometric data with asteroid lightcurves are only available at the CDS via anonymous ftp to cdsarc.u-strasbg.fr (130.79.128.5) or via http://cdsarc.u-strasbg.fr/viz-bin/cat/J/A+A/654/A87

† Deceased.

As a consequence of the scarcity of multi-apparition light curves which are needed for spin and shape reconstruction via light-curve inversion, the statistics of available spin- and shape-modelled asteroids are strongly biased towards faster rotators (Marciniak et al. 2015). This might have implications on our interpretation of the statistical properties of the asteroid population, such as for example the role of the YORP effect (Vokrouhlický et al. 2015) on the spatial distribution of spin axes (Hanuš et al. 2013), or the estimated contribution of tumblers and binaries in various asteroid populations (Ďurech et al. 2020).

Another hidden problem is that most of the well-studied asteroids, especially among slow rotators, are those with large-amplitude light curves (Warner & Harris 2011), caused by an elongated shape, high spin axis inclination, or both. In our survey, described in detail in Marciniak et al. (2015), we addressed two of these biases at the same time, focusing on slow rotators ($P > 12$ h) with maximum amplitudes no larger than 0.25 mag, at least at the target-selection stage. During our study, we found that several targets have somewhat larger amplitudes or shorter periods, but nevertheless we kept these in the final sample of this latter work.

The statistics of asteroids with reliably determined thermal inertia is even more biased. Recompiling data from previous works, as well as new values from Hanuš et al. (2018), Marciniak et al. (2018), and Marciniak et al. (2019), there are currently 36 main-belt slow rotators, compared to 120 fast rotators studied using detailed thermophysical modelling (TPM). This shows that, in terms of studying slow rotators in the infrared, we have only touched the tip of the iceberg.

Thermal inertia ($\Gamma = \sqrt{\kappa\rho c}$) depends on the density of surface regolith ρ, thermal conductivity κ, and heat capacity c. Larger thermal inertia implies coarser regolith composed of grain sizes of the order of millimetres to centimetres, typical for young surfaces of small near-Earth asteroids (NEAs; Gundlach & Blum 2013), while much finer, lunar-like regolith with grain sizes of between 10 and 100 microns is expected at large ($D > 100$ km) main-belt asteroids (see e.g. Delbo' & Tanga 2009, and references therein). This picture might however be complicated by various family formation ages, recent catastrophic events refreshing the surface, or by the presence of surface cohesion forces (Marchi et al. 2012; Rozitis et al. 2014). Also, as more asteroids become thermally characterised we can also understand how thermal processes like thermal cracking (Delbo' et al. 2014; Ravaji et al. 2019) have shaped or are still shaping asteroid surfaces.

However, in light of recent results for two targets studied in situ, Ryugu and Bennu (Okada et al. 2020; Walsh et al. 2019), this standard interpretation of thermal inertia versus surface properties fails; there are boulders on the surface with relatively low thermal inertia, while one would expect regolith. Thermal conductivity, and thus thermal inertia dependance on temperature at various subsurface depths, is another factor to be considered (Hayne et al. 2017). It has been shown that submillimetre flux probes deeper layers, carrying information on the conditions in these layers (Keihm et al. 2012).

Harris & Drube (2016) estimated thermal inertias based on beaming parameters derived from WISE data (Masiero et al. 2011, and references therein) and found that thermal inertia increases with rotation period. This motivated us to add the thermophysical analysis to our study of slow rotators. At first, our results seemed to confirm this hypothesis (Marciniak et al. 2018), as we found large and medium thermal inertia values for the first sample of five targets. Later, with a sample of twice the size, we found a rather wide range of thermal inertia (Marciniak et al. 2019), from very small to medium, similarly to Hanuš et al. (2018), generally not showing any trend with the rotation period. Still, the size of the slow rotators sample with known thermal inertia remains small. In this work we continue our effort to expand this sample employing a different approach, namely the Convex Inversion Thermophysical Model (CITPM, see Sect. 3).

The light-curve inversion method (Kaasalainen et al. 2001) can robustly reproduce asteroid spin and shape, provided the visible data cover a wide range of viewing geometries. However, for targets orbiting close to the ecliptic plane (i.e. most of the main-belt asteroids), the result usually consists of two mirror pole solutions (Kaasalainen & Lamberg 2006; Kaasalainen & Ďurech 2020). These are similar in spin axis ecliptic latitude, but differ in ecliptic longitude: both solutions are roughly 180° apart, and have different associated shape models. One such mirror pole solution sometimes happens to fit thermal data better than the other (see e.g. Delbo' & Tanga 2009). However, this can stem from the high sensitivity of thermal flux to small-scale shape details, and might not point to a truly better spin solution (Hanuš et al. 2015; Kaasalainen & Ďurech 2020). We therefore decided to switch from independent light curve inversion followed by thermophysical modelling of a fixed shape to simultaneous optimisation of both types of data. The method enabling this approach is the CITPM introduced in Ďurech et al. (2017). This method also enables the user to weight two types of data relative to each other to avoid the dominance of one data type over the other. Müller et al. (2017) applied this method for asteroid Ryugu and the derived size, albedo, and thermal inertia are very close to the in situ properties; however, the spin pole was not well determined by this method (probably because of the very low light-curve amplitude and the lack of high-quality measurements).

In Sect. 2, we describe the visible and infrared data used for modelling. Section 3 presents the main features of the method for combined optical and mid-infrared photometric inversion, which is followed in Sect. 4 by a description of the method used to scale the models by multi-chord stellar occultations. The resulting models, with their spin, shape, and thermal parameters with the occultation scaling are presented in Sect. 5. In Sect. 6 we summarise the results and discuss our ideas for future work. All the plots and figures asssociated with the models can be found in the appendix.

2. Visible and infrared data

Data for traditional, dense light curves in the visible range have been gathered in the framework of our long-term photometric campaign conducted since the year 2013, and are described in Marciniak et al. (2015), including target-selection criteria. In short, the aim of the project is to observe a few tens of slowly rotating main-belt asteroids with small brightness variation amplitudes. It involves over 20 observing stations with telescopes of up to 1 m in diameter, including for example TRAPPIST telescopes (Jehin et al. 2011). To compliment these data, we also use data from the *Kepler* Space Telescope in the extended K2 mission (Howell et al. 2014) downlinked within our proposals accepted by *Kepler* and K2 Science Center, as well as publicly available data from TESS (Pál et al. 2020)[1], and Super WASP sky survey (Grice & et al. 2017)[2]. From the latter archive, we only used the best-quality subsets, choosing from targets with Super WASP datapoints already folded into light

[1] https://archive.konkoly.hu/pub/tssys/dr1/
[2] http://asteroids.neilparley.com/asteroids/lc.html

curves. Trimming those vast datasets was necessary because of their abundance and in order to avoid dominance of one apparition over others, but also because of their intrinsic noise. Noisy light curves can sometimes prevent the identification of a unique model solution over the whole dataset. The selection criteria for the best Super WASP light-curve fragments were the lowest photometric scatter and the widest possible range of observing dates.

The great majority of the dense light curve data from our photometric campaign were provided in the form of relative photometry, and the rest were treated as such to ascertain light-curve inversion convergence. Separate light-curve fragments obtained during our observing campaign in the *R* filter or unfiltered were combined to create composite light curves (Figs. E.1–E.66) using the criterion of minimum scatter between data points for initial period determinations. We present the light curves that cover most of the rotation period and show clear brightness variations. For modelling, however, we used all the data described in Table D.1. Determined synodic periods are in agreement in all apparitions, with differences of only a few thousandths due to changes in relative velocity of the observer and the source. The synodic period range from various apparitions, extended at least three times, is a range on which the precise, sidereal period is later searched for in the light-curve inversion procedure.

Composite light curves from various apparitions depict the general character of the asteroid shape (if regular and symmetric, or quite the opposite). Light-curve differences are due to phase-angle effects caused by shadowing on topographic features, and different viewing geometries (aspect angles). Apart from ensuring a full period coverage, sometimes tens of hours long, we paid special attention to covering the widest possible range of ecliptic longitudes and phase angles (see Table D.1), which is a necessary prerequisite for shape reconstruction (Kaasalainen & Ďurech 2020). The small point-to-point scatter of our light curves (see Appendix A), of the order of 0.01 mag down to a few millimagnitudes, captures brightness variations in great detail, even in those cases with very small amplitudes.

Relative photometric data described above were supplemented with the calibrated *V*-band sparse data from the USNO (US Naval Observatory) archive[3]. These are necessary for size and albedo determination in the application of the full CITPM. We decided to exclusively use the USNO archive due to its relatively high quality among the available options. As has been shown by Hanuš et al. (2011) the median accuracy of USNO data is at the level of 0.15 mag.

Thermal infrared data were downloaded from the SBNAF Infrared Database[4] (Szakáts et al. 2020). This database provides expert-reduced data products from major infrared space missions (Akari, Infrared Astronomical Satellite (IRAS), Wide-field Infrared Survey Explorer (WISE), *Herschel*, Midcourse Space Experiment (MSX), and Infrared Space Observatory (ISO)) as well as all the necessary auxiliary information, such as the observing geometry, colour correction, or overall measurement uncertainties. SBNAF Infrared Database was developed within the 'Small Bodies: Near And Far' Horizon 2020 project (Müller et al. 2018). This database stores calibrated flux densities obtained via careful consideration of instrument-specific calibration and processing procedures. All the measurement uncertainty values have been reanalysed for the sake of database consistency, and include contributions from in-band flux density uncertainty, absolute calibration errors, and colour correction uncertainties. The infrared data for our targets came mostly from three missions: WISE (Wright et al. 2010; Mainzer et al. 2011a) at 11.1 and 22.64 μm, Akari (Usui et al. 2011) at 9 and 18 μm, and IRAS (Neugebauer et al. 1984) at 12, 25, 60 and 100 μm, occasionally supplemented with data from MSX (Egan et al. 2003) at 8.28, 12.13, 14.65, and 21.34 μm, where available. All the infrared datapoints were used, except in specific single cases where clear outliers were detected that were unable to be fitted by any of the models. Also, because of the large size of some targets resulting in large infrared flux, sometimes a subset or all WISE data at 11 μm were partially saturated, and could not be used in our analysis.

[3] Downloaded from AstDys https://newton.spacedys.com/astdys2/index.php?pc=3.0

[4] https://ird.konkoly.hu/

3. Convex inversion thermophysical model

To fit optical light curves and thermal infrared data, we used a combined inversion of both data types developed by Ďurech et al. (2017) called the convex inversion thermophysical model. The method combines convex inversion of light curves (Kaasalainen et al. 2001) with a thermophysical model (Lagerros 1996, 1997, 1998). The shape of an asteroid is parametrized by coefficients of spherical functions that describe a convex polyhedron of size D with typically hundreds of surface facets. For each facet, a 1D heat diffusion equation is solved to compute its temperature and infrared flux at the time of observation. The response of the surface to solar radiation is parametrized by the thermal inertia Γ, surface roughness (described by spherical craters of varying both the fraction of surface coverage f, and the opening angle γ_c), and light-scattering properties. For emissivity, a fixed value of 0.9 is used, following a standard approach (e.g. Lim et al. 2005). Instead of using absolute magnitude, Bond albedo, and geometric albedo – which are only unambiguously defined for a sphere – we use Hapke's light-scattering model (Hapke 1981, 1984, 1986), from which any albedos can be directly computed. To tie the reflectance of the surface with the size of the asteroid, absolutely calibrated photometry is needed. Because most of the light curves we collected are provided as the relative photometry, we also use the calibrated *V*-band photometry from the USNO that covers a sufficiently wide range of solar phase angles. Parameters of Hapke's model can be optimised to fit the phase curve. The merit function that we minimise is a sum $\chi^2_{\rm VIS} + w\chi^2_{\rm IR}$ of χ^2 values for optical and thermal data. The relative weight w is iteratively set such that (in an ideal case) the fit to light curves is as good as without thermal data, and the fit to thermal data is good, that is, the normalised $\chi^2_{\rm IR}$ is ∼1. The advantage here is that the spin and shape model optimised against visible light curves only in most cases would not be optimal in the thermal radiation, as shown by Hanuš et al. (2015) and Hanuš et al. (2018); here it is optimised to fit both types of data.

The visual part of χ^2 is computed as

$$\chi^2_{\rm VIS} = \sum_{j=1}^{N-1} \sum_i \left(\frac{L^{\rm obs}_{i,j}}{\bar{L}^{\rm obs}_j} - \frac{L^{\rm model}_{i,j}}{\bar{L}^{\rm model}_j} \right)^2 + 0.2 \sum_i \left(\frac{L^{\rm obs}_{i,N} - L^{\rm model}_{i,N}}{\bar{L}^{\rm obs}_N} \right)^2 ,$$

where N is the total number of light curves, and $L_{i,j}$ is the brightness (in arbitrary intensity units, not magnitudes) of the ith point of the jth light curve. The normalisation by the mean brightness of the jth light curve $\bar{L}_j$ means that we treat all $N-1$ light curves as relative and that we neglect differences in photometric

Table 1. Ancillary information on the data and physical properties of our targets.

Asteroid	N_{app}	N_{lc}	N_I	N_A	N_{W3}	N_{W4}	D_{WISE} [km]	Taxonomic type
(108) Hecuba	8	59	15	7	13	13	75.498	S
(202) Chryseis	7	70	7	8		12	97.948	S
(219) Thusnelda	6	116	18	6		19	38.078	S
(223) Rosa	7	58	20	5		12	83.394	X
(362) Havnia	7	38		9		13	89.202	XC
(478) Tergeste	6	48	27	8	9	9	84.975	S
(483) Seppina	8	56	34	12	12	12	84.975	S
(501) Urhixidur	7	61	11	8	11	11	85.404	C
(537) Pauly	7	50	8	9	6	6	52.330	DU
(552) Sigelinde	6	65	8	6	4		(77.56)	C
(618) Elfriede	9	68	17	5		12	131.165	C
(666) Desdemona	7	60	21	5	13	13	31.485	S
(667) Denise	5	40	21	5	15	13	88.630	C
(780) Armenia	8	95	24	7		12	102.257	C
(923) Herluga	7	51	12	8	16	16	37.638	C
(995) Sternberga	7	81	22	6	11	11	22.350	S

Notes. The first two columns contain asteroid name and the number of apparitions N_{app} during which the N_{lc} of visible light curves were obtained. The next part of the table details the infrared dataset: the number of points provided by space observatories IRAS N_I, Akari N_A, and WISE in W3 and W4 bands: N_{W3}, and N_{W4} respectively. For comparison of the diameters and albedos obtained in this work (see Table 2), the diameters D_{WISE} from WISE spacecraft (Mainzer et al. 2011b; Masiero et al. 2011) and taxonomic types are added (Bus & Binzel 2002a,b, and Tholen 1989). Diameter in parentheses, due to a lack of size determination from WISE, comes from IRAS survey results (Tedesco et al. 2004).

accuracy between them. The only exception is calibrated photometry in V filter from USNO (the Nth light curve), for which we directly compare the observed flux with that predicted by our model without normalising by $\bar{L}_j^{obs}$ and $\bar{L}_j^{model}$ separately. The empirical factor of 0.2 gives less weight to USNO data which is intentional because these have larger errors.

For thermal data, errors of individual measurements are known, and so the thermal part of the χ^2 is computed classically as

$$\chi^2_{IR} = \sum_i \left(\frac{F_i^{obs} - F_i^{model}}{\sigma_i} \right)^2 ,$$

where F_i is observed or modelled flux and σ_i is the error of the measurement. By dividing χ^2_{IR} by the number of degrees of freedom, we get reduced χ^2_{red}, which we use in Sect. 5 when presenting our results.

4. Occultation fitting

For three targets of our current sample there were good quality, multi-chord stellar occultations available in the PDS archive[5] (Herald et al. 2019, 2020). More recent occultation results were downloaded from the archive of the Occult programme[6]. We used them to independently scale the shape models obtained here, using the method described in Ďurech et al. (2011), in order to: compare obtained sizes with those from thermal fitting; confirm the shape silhouette; and if possible, identify the preferred pole solution (see Figs. C.1–C.3).

When scaling the models with occultations, we computed the orientation of the model for the time of occultation and projected the model on the fundamental plane (sky-plane projection). Because all models are convex, their silhouettes are also convex. We then iteratively searched for a scale of the silhouette that would provide the best match with chords. The mutual shift between the silhouette and the chords was described by two free parameters that were also optimised. We used the χ^2 minimisation, where the difference between the silhouette and the chords was measured as a distance in the fundamental plane between the ends of the chords and the silhouette (measured along the direction of the chord). We rejected the solutions in which a negative chord (no occultation was observed) intersected the silhouette.

5. Results

Table 1 provides the ancillary information on the visible and thermal datasets: number of apparitions and separate light curves, numbers of thermal measurements from separate missions, and WISE diameters from Mainzer et al. (2011b); Masiero et al. (2011) to be compared with diameters obtained in this work (see Table 2). We also cite taxonomic type following Bus & Binzel (2002a,b) and Tholen (1989), for a consistency check with our values for albedo (consistent in all cases).

Table 2 summarises all the rotational and thermophysical properties of the targets studied here. First the spin solution is presented, usually with its mirror counterpart. The quality of the fit to light curves in the visible range is given in Col. 5. The second part of the table presents the radiometric solution based on combined data from three infrared missions, the radiometric diameter, geometric albedo, thermal inertia, and the reduced χ^2 of modelled versus observed fluxes. Lastly, the table contains the average heliocentric distance at which thermal measurements were taken, and thermal inertia reduced to one astronomical unit, using the formula (Rozitis et al. 2018):

$$\Gamma_{1AU} = \Gamma(r) r^{\alpha}, \quad (1)$$

[5] http://sbn.psi.edu/pds/resource/occ.html
[6] http://www.lunar-occultations.com/iota/occult4.htm

Table 2. Spin parameters and thermophysical characteristics of asteroid models obtained in this work.

Asteroid	Pole		P	vis. dev	D	p_V	Γ	χ^2_{red}	r_{hel}	Γ_{1AU}
	λ_p[°]	β_p[°]	[h]	[mag]	[km]		[SI units]	IR	[AU]	[SI units]
(108) Hecuba	181 ± 2	+42 ± 5	14.25662 ± 0.00003	0.013	69^{+3}_{-1}	$0.24^{+0.04}_{-0.01}$	35^{+25}_{-30}	1.08	3.18 ± 0.10	85
	352 ± 1	+39 ± 6	14.25662 ± 0.00003	0.012	70 ± 2	$0.24^{+0.04}_{-0.01}$	40 ± 30	1.10	3.18 ± 0.10	95
(202) Chryseis	94 ± 1	−49 ± 4	23.67025 ± 0.00006	0.012	90^{+4}_{-3}	$0.22^{+0.03}_{-0.01}$	<180	0.35	2.96 ± 0.15	<405
	261 ± 1	−34 ± 4	23.67028 ± 0.00004	0.012	90^{+3}_{-3}	$0.22^{+0.01}_{-0.01}$	<180	0.36	2.96 ± 0.15	<405
(219) Thusnelda	300 ± 10	−66 ± 10	59.7105 ± 0.0001	0.014	44^{+2}_{-4}	$0.19^{+0.04}_{-0.01}$	<120	0.80	2.24 ± 0.42	<220
(223) Rosa	22 ± 3	+18 ± 18	20.2772 ± 0.0003	0.012	69^{+9}_{-3}	$0.033^{+0.006}_{-0.004}$	<300	0.72	2.99 ± 0.12	<680
	203 ± 2	+26 ± 15	20.2769 ± 0.0003	0.012	70^{+6}_{-2}	$0.032^{+0.007}_{-0.003}$	<300	0.78	2.99 ± 0.12	<680
(362) Havnia	14 ± 2	+33 ± 2	16.92665 ± 0.00003	0.017	92^{+6}_{-5}	$0.044^{+0.006}_{-0.004}$	<180	0.80	2.64 ± 0.04	<370
	208 ± 8	+35 ± 4	16.92668 ± 0.00003	0.017	91^{+8}_{-3}	$0.046^{+0.004}_{-0.008}$	<200	0.67	2.64 ± 0.04	<410
(478) Tergeste	2 ± 5	−38 ± 8	16.10308 ± 0.00004	0.019	83 ± 4	$0.16^{+0.05}_{-0.01}$	2^{+45}_{-1}	0.94	3.05 ± 0.10	5
	216 ± 7	−62 ± 4	16.10312 ± 0.00004	0.016	81^{+5}_{-4}	$0.18^{+0.03}_{-0.02}$	26 ± 25	0.88	3.05 ± 0.10	60
(483) Seppina	127 ± 3	+47 ± 3	12.720968 ± 0.000004	0.019	73^{+5}_{-2}	$0.16^{+0.04}_{-0.01}$	17^{+23}_{-12}	0.80	3.45 ± 0.14	45
	356 ± 4	+60 ± 3	12.720977 ± 0.000002	0.019	74^{+4}_{-2}	$0.16^{+0.04}_{-0.01}$	23^{+17}_{-18}	0.83	3.45 ± 0.14	60
(501) Urhixidur	49 ± 40	+84 ± 12	13.17203 ± 0.00002	0.019	77^{+5}_{-2}	$0.051^{+0.003}_{-0.008}$	4^{+35}_{-2}	0.53	3.20 ± 0.32	10
	262 ± 24	+66 ± 11	13.17203 ± 0.00001	0.018	82^{+2}_{-4}	$0.050^{+0.002}_{-0.007}$	13^{+30}_{-11}	0.53	3.20 ± 0.32	31
(537) Pauly	32 ± 3	+43 ± 6	16.29601 ± 0.00002	0.018	47^{+1}_{-2}	$0.26^{+0.03}_{-0.02}$	11^{+30}_{-10}	0.70	2.96 ± 0.45	25
	214 ± 4	+60 ± 9	16.29597 ± 0.00001	0.018	46 ± 2	$0.25^{+0.05}_{-0.02}$	13^{+50}_{-12}	0.74	2.96 ± 0.45	29
(552) Sigelinde	8 ± 24	+73 ± 9	17.14963 ± 0.00001	0.017	88^{+10}_{-5}	$0.030^{+0.011}_{-0.007}$	3^{+55}_{-2}	0.97	3.26 ± 0.09	7
	189 ± 18	+60 ± 17	17.14962 ± 0.00003	0.017	91^{+7}_{-13}	$0.029^{+0.005}_{-0.007}$	2^{+55}_{-1}	1.13	3.26 ± 0.09	5
(618) Elfriede	102 ± 20	+64 ± 7	14.79565 ± 0.00002	0.015	145^{+15}_{-13}	$0.047^{+0.010}_{-0.003}$	<350	0.28	3.32 ± 0.10	<860
	341 ± 13	+49 ± 6	14.79564 ± 0.00002	0.015	146^{+15}_{-16}	$0.053^{+0.002}_{-0.009}$	<400	0.32	3.32 ± 0.10	<980
(666) Desdemona	10 ± 4	+39 ± 5	14.60795 ± 0.00008	0.022	$28.4^{+0.9}_{-0.8}$	$0.111^{+0.007}_{-0.009}$	<70	0.83	2.79 ± 0.34	<150
	174 ± 3	+36 ± 11	14.60796 ± 0.00003	0.022	$28.3^{+0.9}_{-1.0}$	$0.116^{+0.002}_{-0.014}$	<100	0.77	2.79 ± 0.34	<215
(667) Denise	15 ± 25	−83 ± 6	12.68499 ± 0.00003	0.024	83^{+4}_{-2}	0.051 ± 3	13^{+17}_{-8}	1.19	3.36 ± 0.38	32
	237 ± 3	*−23 ± 6*	*12.68497 ± 0.00003*	0.025	82^{+5}_{-2}	$0.051^{+0.002}_{-0.004}$	6^{+24}_{-1}	1.16	3.36 ± 0.38	15
(780) Armenia	144 ± 7	−44 ± 11	19.88453 ± 0.00007	0.014	98^{+2}_{-3}	$0.042^{+0.005}_{-0.003}$	<300	0.47	3.00 ± 0.10	<680
	293 ± 3	−23 ± 6	19.88462 ± 0.00009	0.015	102^{+3}_{-2}	0.038 ± 0.003	<250	0.63	3.00 ± 0.10	<570
(923) Herluga	218 ± 9	−68 ± 5	29.72820 ± 0.00002	0.022	$36.2^{+0.4}_{-1.5}$	$0.047^{+0.004}_{-0.003}$	37^{+15}_{-36}	0.92	2.73 ± 0.40	80
	334 ± 7	−52 ± 3	29.72826 ± 0.00001	0.023	$34.1^{+0.8}_{-1.0}$	$0.050^{+0.002}_{-0.003}$	14^{+35}_{-13}	0.95	2.73 ± 0.40	30
(995) Sternberga	27 ± 3	−20 ± 6	11.19511 ± 0.00012	0.019	$25.5^{+1.1}_{-1.4}$	$0.22^{+0.03}_{-0.04}$	<100	0.85	2.73 ± 0.30	<210
	222 ± 4	−26 ± 5	11.19512 ± 0.00008	0.019	$25.2^{+1.1}_{-0.9}$	$0.226^{+0.005}_{-0.032}$	<120	0.84	2.73 ± 0.30	<250

Notes. The columns contain asteroid name, J2000 ecliptic coordinates λ_p, β_p of the spin solution, with mirror pole solution in the second row, sidereal rotation period P, and the deviation of model fit to those light curves (including fit to sparse data). The next part of the table details the radiometric solution for combined data: surface-equivalent size D, geometric albedo p_V, thermal inertia Γ in J m^{-2} s$^{-1/2}$ K^{-1} (SI) units, and the reduced chi-square of the best-fit (χ^2_{red}). The last two columns give average heliocentric distance of thermal infrared observations r_{hel} with the standard deviation, and thermal inertia normalised to 1 AU Γ_{AU} calculated according to Eq. (1). Numbers in italics mark the pole solution of (667) Denise clearly rejected by occultation fitting.

where the α exponent is equal to 0.75, which takes into account a radiative conduction term in thermal conductivity. Different exponents are also possible (Rozitis et al. 2018), but here we opted for the most widely used value to facilitate comparison with previous works (see the discussion in Alí-Lagoa et al. 2020; Szakáts et al. 2020).

In Appendix A we present the plots of χ^2_{red} versus thermal inertia for various combinations of surface roughness and optimised size (Figs. A.1 – A.16). To transform various combinations of crater coverage and opening angle to rms of surface roughness, we used the formula no. 20 from Lagerros (1998). In these figures, f is the fraction of crater coverage, and the plots show the χ^2_{red} of the crater opening angle that minimised the χ^2_{red} for that value of f. The horizontal line is the acceptance threshold for χ^2_{red} values, depending classically on the number of IR measurements and best χ^2_{red} value: we accept all the solutions

Table 3. Diameters of equivalent volume spheres for CITPM shape models fitted to stellar occultations.

Target	Pole 1	Pole 2
362 Havnia	84 ± 1 km	88 ± 1 km
618 Elfriede	145 ± 7 km	155 ± 2 km
667 Denise	83 ± 2 km	Rejected

Table 4. Previously published spin parameters for targets studied here.

Asteroid	Pole		P	Reference
	λ_p[°]	β_p[°]	[h]	
(108) Hecuba	*79* ± 1	*+13* ± 11	–	Blanco & Riccioli (1998)
	259 ± 7	*−6* ± 7	–	Blanco & Riccioli (1998)
(219) Thusnelda	*253* ± 4	−69 ± 4	59.712 ± 0.002	Ďurech et al. (2020)
(362) Havnia	96^{+3}_{-2}	$+39^{+7}_{-2}$	$16.918773^{+0.00003}_{0.000006}$	Wang et al. (2015)
	273^{+1}_{-6}	$+40^{+1}_{-10}$	$16.918935^{+0.00001}_{0.00004}$	Wang et al. (2015)
(478) Tergeste	2 ± 2	−42 ± 3	16.10308 ± 0.00003	Marciniak et al. (2018)
	216 ± 6	−56 ± 4	16.10308 ± 0.00003	Marciniak et al. (2018)
(483) Seppina	–	+42 ± 20	12.72081 ± 0.00006	Ďurech et al. (2020)
(537) Pauly	*290* ± 31	+40 ± 31	–	Blanco et al. (2000)
	31 ± 12	+32 ± 10	16.2961 ± 0.0005	Hanuš et al. (2016)
	211 ± 16	+51 ± 10	16.2961 ± 0.0005	Hanuš et al. (2016)
(552) Sigelinde	–	+48 ± 19	17.1494 ± 0.0002	Ďurech et al. (2020)
(618) Elfriede	113 ± 3	+54 ± 3	14.7952 ± 0.0001	Ďurech et al. (2020)
	323 ± 1	*+25* ± 3	14.7952 ± 0.0001	Ďurech et al. (2020)
(666) Desdemona	–	+12 ± 22	14.6080 ± 0.0002	Ďurech et al. (2020)
(667) Denise	40 ± 6	−86 ± 3	12.6848 ± 0.0002	Ďurech et al. (2020)
(923) Herluga	188 ± 5	−60 ± 5	29.7282 ± 0.0007	Ďurech et al. (2020)

Notes. The columns contain asteroid name, J2000 ecliptic coordinates λ_p, β_p of the spin solution, sidereal rotation period P, and the reference. Values in italics denote solutions substantially differing from the ones obtained in the current paper.

with $\chi^2_{red} < (1 + \sigma)$, where $\sigma = \sqrt{2\nu}/\nu$, with ν being the number of degrees of freedom. For a few targets with a value of best χ^2_{red} much below 1, probably due to unresolvable mutual parameter correlations, we used an empirical approach by Hanuš et al. (2015) to define that threshold: $\chi^2_{red} < (\chi^2_{min} + \sigma)$.

For each target we also present the fit to WISE W3 and W4 thermal light curves, whenever available (Figs. B.1–B.25). Due to the scarce character of Akari and IRAS data (only 1–3 points per band on average), the model fits to them are not shown. The plots present the results for only one of two mirror pole solutions (the other pole gave very similar results, as indicated by χ^2_{red} values from Table 2).

As a consistency check, we re-ran one of our previous targets, (478) Tergeste, now using the CITPM. In one of our earlier works (Marciniak et al. 2018), this target was spin- and shape-modelled, and then the resulting models that best fitted the light curves in the visible were applied in TPM procedures. In that work we obtained thermal inertia in the range of 30–120 J m^{-2} s$^{-1/2}$ K^{-1} (SI units), and reduced χ^2 of models fit to infrared data of 2.18 and 1.53 for poles 1 and 2, respectively, revealing a strong preference for one of the spin and shape solutions, but also problems with fitting all the thermal data. New simultaneous optimisation on the same visible and infrared datasets performed here led to a somewhat different model. Most notably, the reduced χ^2 decreased substantially to 0.94 for pole 1, and 0.88 for pole 2, and so some preference for one spin solution remained, and thermal inertia shifted to smaller values: 1–50 SI units. To further check, we modelled the IR data using the new shape models with the classical TPM approach (Lagerros 1996, 1997, 1998) and found a consistent solution.

The fit to visible light curves remained similarly good with both approaches, and the spin axis coordinates, size, and albedo agreed with the original ones within the error bars. In summary, the CITPM method enabled us to find a much better combination of spin, shape, and thermal parameters than the two-step approach used originally.

The CITPM method provides models for several targets for which previous analyses with the classical TPM method failed; for example a unique and stable solution was found for (487) Seppina. For (666) Desdemona, we constrained the size and albedo to a narrow range, while thermal inertia still remains uncertain. Furthermore, for two targets (667, 995), additional calibrated data used in the CITPM improved the solution of inertia tensors, which were previously erroneous (i.e. excessively stretched along the spin axis). Also, we were able to find more precisely constrained dimensions along the spin axis for the shape models for all the other targets, which is an area of frequent weakness in shape models based exclusively on relative photometry.

Independent confirmation of the robustness of our models also comes from fitting the models to stellar occultation chords. The results of occultation fitting are presented in Table 3, and in Figs. C.1–C.3, which show the instantaneous silhouette of the shape model on the η, ξ sky plane scaled in kilometres. Table D.2 lists the occultation observers and sites.

Spin and shape solutions had already been determined and published in the literature for some of our targets, while in some cases only some of the parameters were available. In Table 4 we cite their spin axis coordinates and sidereal periods, if available, together with their reference. Comparison with our results in Table 2 shows a general agreement, with the exception of (108)

Hecuba modelled by Blanco & Riccioli (1998), (362) Havnia modelled by Wang et al. (2015), and (537) Pauly modelled by Blanco et al. (2000) based on different shape approximations. Parameters strongly differing from the solutions obtained in this work are marked in italics in Table 4. Within consistent solutions, the differences in sidereal periods are sometimes of the order of a few 10^{-4} h, which may appear small, but might be noticeable after a few apparitions. In the sections below, we focus on a few specific targets in more detail.

5.1. (362) Havnia

There were problems with some photometric data for this target. Firstly, data obtained by Harris & Young (1980) were published in the APC archive as a composite light curve, with an incorrect period of 18 h. As a consequence, only one out of three light curves could be used, the one with original timings. This is a general problem with some early asteroid light curves in the archives, and special attention must be paid when using them. Other problems were caused by Super WASP data. Although in many cases these serendipitously gathered data provided good light curves from desired geometries, in this case their intrinsic noise made it impossible to find a unique spin and shape solution. After removing most of the Super WASP light curves for Havnia and keeping only the five best ones (Fig. E.18), the uniqueness of the solution greatly improved. This demonstrates that the light curve inversion method is quite sensitive to noise in the data.

A spin and shape model of Havnia previously published by Wang et al. (2015) was based on a light-curve inversion using the Monte Carlo method on data from four apparitions (see Table 4), while our model was based on (visible) light curves from seven apparitions. The model by Wang et al. (2015) agrees with the model obtained here only in spin axis latitude (see Table 2), whereas the longitudes are substantially different. Sidereal periods might appear similar at first sight, but they would lead to a large divergence of extrema timings over just two apparitions.

Our model is characterised by a rather wide range of thermal inertia values due to a poor infrared dataset (only data from Akari and WISE W4 were available; see N values in Table 1), but Fig. A.5 shows a clear minimum around $\Gamma = 100$ SI units. Unfortunately, all WISE W3 data had to be removed because of partial saturation. Even keeping only their best subset led to divergence.

There is a four-chord stellar occultation from the year 2017 available in the PDS archive. Both of our spin and shape solutions fit this event very well, with all chords crossing close to the centre of the body (see Fig. C.1), resulting in volume-equivalent sizes a few percent smaller than the sizes provided by the CITPM method (compare D values in Tables 3 and 2). The small ±1 km error in the occultation diameter is only a formal uncertainty determined via bootstrapping separate chords and repeating the fitting procedure multiple times. However, the real uncertainty must be larger because of the uncertainty on the shape model itself.

5.2. (537) Pauly

Spin and shape solutions for (537) Pauly have already been published by Blanco et al. (2000) and Hanuš et al. (2016). The results from the latter work are consistent with ours (see Tables 2 and 4), although our model of Pauly is made using many more dense light curves and also a richer set of thermal data (+9 Akari points), and via simultaneous optimisation of both data types. Later, (537) Pauly was also analysed with the TPM via the data bootstrapping method (Hanuš et al. 2018). Our size determinations (46 ± 2 km, and 47 ± 4 km) are somewhat larger than 40.7 ± 0.8 km by Hanuš et al. (2018), but the thermal inertia and albedo values agree. Our $\chi^2_{\rm red}$ IR residuals are smaller than in the previous model (0.7 vs. 1.1). The difference in size might stem from the elongated shape of this target, and the smaller set of infrared measurements in Hanuš et al. (2018), capturing the target within a limited range of rotation phases, which might have led to underestimation of the size in previous study.

5.3. (618) Elfriede

There were as many as four different stellar occultations by this target, each containing from two to four chords (Fig. C.2). However, these data did not help us reject any of our two models and we take pole 2 ($\lambda_{\rm p} = 341°, \beta_{\rm p} = +49°$) as the preferred solution based simply on its slightly lower χ^2.

In this case, the occultation size agrees exactly for pole 1 with the radiometric size, while for pole 2 it is a few percent larger (see Tables 3 and 2), but still within the radiometric error bars. Our results, though self-consistent, are in disagreement with most previous size determinations for 618 Elfriede. The occultation-determined size for pole 2 (155 ± 2 km) is almost 30% larger than Akari (121.54 km) and IRAS (120.29 km) determinations (Usui et al. 2011; Tedesco et al. 2004), and 18% larger than the diameter given by WISE (131.165 km Mainzer et al. 2011b). For pole 1, the size disagreement is less pronounced (20 and 11% respectively) and is even compatible with the WISE diameter within the error bars.

In summary, as the present study is the first to take a comprehensive and multi-technique approach to analysing this target (rich photometric set simultaneously combined with infrared data from three missions, plus independent occultation fitting), the size determined here (14–155 km) can probably be considered the most reliable.

5.4. (667) Denise

For asteroid (667) Denise there were three good stellar occultations – with one containing as many as ten positive chords – thanks to a very successful European campaign (observers are acknowledged in Table D.2). Although both pole solutions are formally acceptable from the thermophysical point of view (both present in Table 2), the occultation fitting clearly enabled us to reject the solution for pole 2 (see Fig. C.3), which is marked with italics in Table 2. The size determined from occultations (83 ± 2 km) is the same as the radiometric size (83^{+4}_{-2} km). The CITPM method proved to be robust and accurate, and provided the most accurate parameters in the case of dense stellar occultation chords.

6. Conclusions and future work

We fully characterised spin, shape, and thermal properties of 16 main-belt asteroids from the group that until recently has been neglected because of observing selection effects. The multi-apparition targeted observing campaign together with good-quality infrared data, especially from the WISE spacecraft, led to consistent spin and shape models accompanied by precise size and albedo determinations, and thermal inertia being determined for most of the targets for the first time. Thanks to simultaneous use of both visible and infrared data, our shape models are

optimal in terms of reproducing both types of data well. Also, the CITPM gained additional evidence for its robustness, providing an optimal solution in one of the cases, as confirmed by an independent method. The set contains two updated models (478 Tergeste, and 537 Pauly), and a few targets with partial solutions due to the scarcity of infrared data.

With this work we increase the number of slow rotators with thermal inertia determined from detailed thermophysical modelling by 40%. It is necessary to enlarge the pool of such well-studied targets so that we can gain more insight into different asteroid groups and families separately and explore links between thermal properties, surface material properties, and family formation ages (Harris & Drube 2020). Most targets presented here do not belong to any collisional family (with the exception of 923 Herluga and 995 Sternberga, both from the Eunomia family, and also 618 Elfriede and 780 Armenia, each having their own small, compact family), and so their low thermal inertia was expected.

Our target sizes span the range from a few tens of kilometres to over 100 km, with most of the determinations being within 10% of previous determinations based on WISE data only, and the NEATM thermal model (Harris 1998). Sizes determined for a few targets (223, 552, 618) differ by more, although our approach (including infrared data combined with spin and shape models) has been shown to be robust. We therefore consider our results to be most reliable. Furthermore, obtained albedo values agree with previously published taxonomic classifications.

The thermal inertia values determined here are <100 SI units for most targets, indicating the presence of a thick layer of insulating regolith on most of these bodies. These values of thermal inertia reduced to 1 AU display no trend with size, because our current targets are well within the size range where largely different thermal inertias have been found in previous works (see Fig. 7 in Hanuš et al. 2018). The correlation between thermal inertia and size found by Delbo' et al. (2007) could only be evident if our sample also contained asteroids smaller than 10 km, these being too faint for our photometric campaign on small telescopes.

We also found no evidence to support the hypothesis that thermal inertia increases with rotation period (e.g. Harris & Drube 2016). Our results are in agreement with those of (Marciniak et al. 2019) and Hanuš et al. (2018). Biele et al. (2019) showed that a fine-grained, highly porous surface layer of just a few millimetres thick can hide thermal signatures of denser, more thermally conductive layers due to its relatively small thermal skin depth (d_s) of a few millimetres, while to see signatures of the denser layers would require probing a centimetre range. However, despite their longer rotation periods (11–59 h) compared to the typical light-curve inversion and TPM targets found in the literature, the thermal skin depths of our targets calculated according to the formula given by Spencer et al. (1989) still lie in the range of a few millimetres. The cases with large thermal inertia error bars could still be compatible with d_s up to 3.5 cm, however all the values below it are equally possible, and so this cannot be used for drawing firm conclusions.

Furthermore, we did not find any correlation between thermal inertia and spin axis inclination, or any specific problems with fitting more inclined targets, which must experience seasonal cycles of heating and cooling. However, our thermal inertia determinations, as is often the case, are burdened with large uncertainties. It is possible that the trend linking thermal inertia and rotation period simply eludes us in our investigations, as precise thermal inertia determinations might be hampered by slow rotation, decreasing the thermal lag. For future studies, it will be beneficial to focus on targets with thermal measurements from WISE spacecraft obtained at epochs separated in time by as much as possible (longer than ~100 days). This should help to constrain thermal inertia better thanks to more varied viewing geometries, enabling comparison of thermal flux from for example pre- and post-opposition geometries.

Our scaled spin and shape models and their thermal parameters are available in the new version of DAMIT (Database for Asteroid Models from Inversion Techniques; Ďurech et al. 2010)[7], and data tables with photometry in the visible are available via the CDS.

Acknowledgements. This work was was initiated with the support from the National Science Centre, Poland, through grant no. 2014/13/D/ST9/01818; and from the European Union's Horizon 2020 Research and Innovation Programme, under Grant Agreement no 687378 (SBNAF). The work of J.D. was supported by the grant 20-08218S of the Czech Science Foundation. A.P. and R.S. have been supported by the K-125015 grant of the National Research, Development and Innovation Office (NKFIH), Hungary. This project has been supported by the Lendület grant LP2012-31 of the Hungarian Academy of Sciences. This project has been supported by the GINOP-2.3.2-15-2016-00003 grant of the Hungarian National Research, Development and Innovation Office (NKFIH). L.M. was supported by the Premium Postdoctoral Research Program of the Hungarian Academy of Sciences. The research leading to these results has received funding from the LP2018-7/2020 Lendület grant of the Hungarian Academy of Sciences. The work of T.S.-R. was carried out through grant APOSTD/2019/046 by Generalitat Valenciana (Spain). This work was supported by the MINECO (Spanish Ministry of Economy) through grant RTI2018-095076-B-C21 (MINECO/FEDER, UE). E. P. acknowledges the Europlanet 2024 RI project funded by the European Union's Horizon 2020 Research and Innovation Programme (Grant agreement No. 871149). This article is based on observations obtained at the Observatório Astronômico do Sertão de Itaparica (OASI, Itacuruba) of the Observatório Nacional, Brazil. F.M. would like to thank the financial support given by FAPERJ (Process E-26/201.877/2020). E.R., P.A., H.M., M.E. and J.M. would like to thank CNPq and CAPES (Brazilian agencies) for their support through diverse fellowships. Support by CNPq (Process 305409/2016-6) and FAPERJ (Process E-26/202.841/2017) is acknowledged by D.L. The Joan Oró Telescope (TJO) of the Montsec Astronomical Observatory (OAdM) is owned by the Catalan Government and operated by the Institute for Space Studies of Catalonia (IEEC). This article is based on observations made in the Observatorios de Canarias del IAC with the 0.82 m IAC80 telescope operated on the island of Tenerife by the Instituto de Astrofísica de Canarias (IAC) in the Observatorio del Teide. This article is based on observations made with the SARA telescopes (Southeastern Association for Research in Astronomy), whose nodes are located at the Observatorios de Canarias del IAC on the island of La Palma in the Observatorio del Roque de los Muchachos; Kitt Peak, AZ under the auspices of the National Optical Astronomy Observatory (NOAO); and Cerro Tololo Inter-American Observatory (CTIO) in La Serena, Chile. This project uses data from the SuperWASP archive. The WASP project is currently funded and operated by Warwick University and Keele University, and was originally set up by Queen's University Belfast, the Universities of Keele, St. Andrews, and Leicester, the Open University, the Isaac Newton Group, the Instituto de Astrofisica de Canarias, the South African Astronomical Observatory, and by STFC. TRAPPIST-South is a project funded by the Belgian Fonds (National) de la Recherche Scientifique (F.R.S.-FNRS) under grant PDR T.0120.21. TRAPPIST-North is a project funded by the University of Liège, in collaboration with the Cadi Ayyad University of Marrakech (Morocco). E. Jehin is FNRS Senior Research Associate. Funding for the *Kepler* and K2 missions are provided by the NASA Science Mission Directorate. The data presented in this paper were obtained from the Mikulski Archive for Space Telescopes (MAST). STScI is operated by the Association of Universities for Research in Astronomy, Inc., under NASA contract NAS5-26555. Support for MAST for non-HST data is provided by the NASA Office of Space Science via grant NNX09AF08G and by other grants and contracts. Data from Pic du Midi Observatory have been obtained with the 0.6-m telescope, a facility operated by Observatoíre Midi Pyrénées and Association T60, an amateur association. We acknowledge the contributions of the occultation observers who have provided the observations in the dataset. Most of those observers are affiliated with one or more of: European Asteroidal Occultation Network (EAON), International Occultation Timing Association (IOTA), International Occultation Timing Association European Section (IOTA/ES), Japanese Occultation Information Network (JOIN), and Trans Tasman Occultation Alliance (TTOA).

[7] https://astro.troja.mff.cuni.cz/projects/damit/

References

Alí-Lagoa, V., Müller, T. G., Kiss, C., et al. 2020, A&A, 638, A84
Barucci, M. A., di Martino, M., & Fulchignoni, M. 1992, AJ, 103, 1679
Benishek, V., & Pilcher, F. 2009, Minor Planet Bull., 36, 167
Biele, J., Kührt, E., Senshu, H., et al. 2019, Prog. Earth Planet. Sci., 6, 48
Blanco, C., & Riccioli, D. 1998, A&AS, 131, 385
Blanco, C., Cigna, M., & Riccioli, D. 2000, Planet. Space Sci., 48, 973
Brinsfield, J. W. 2009, Minor Planet Bull., 36, 64
Bus, S. J., & Binzel, R. P. 2002a, Icarus, 158, 146
Bus, S. J., & Binzel, R. P. 2002b, Icarus, 158, 106
Čapek, D., & Vokrouhlický, D. 2010, A&A, 519, A75
Delbo', M., & Tanga, P. 2009, Planet. Space Sci., 57, 259
Delbo', M., dell'Oro, A., Harris, A. W., Mottola, S., & Mueller, M. 2007, Icarus, 190, 236
Delbo', M., Libourel, G., Wilkerson, J., et al. 2014, Nature, 508, 233
Delbo', M., Mueller, M., Emery, J. P., Rozitis, B., & Capria, M. T. 2015, Asteroid V, Asteroid Thermophysical Modeling (Tucson: University of Arizona Press), 107
Ďurech, J., Sidorin, V., & Kaasalainen, M. 2010, A&A, 513, A46
Ďurech, J., Kaasalainen, M., Herald, D., et al. 2011, Icarus, 214, 652
Ďurech, J., Delbo', M., Carry, B., Hanuš, J., & Alí-Lagoa, V. 2017, A&A, 604, A27
Ďurech, J., Tonry, J., Erasmus, N., et al. 2020, A&A, 643, A59
Egan, M. P., Price, S. D., & Kraemer, K. E. 2003, AAS Meeting Abs., 203, Abstracts, 57.08
Grice, J., Snodgrass C., Green S., Parley N., & Carry, B. 2017, in Asteroids, Comets, meteors (USA: HarperCollins)
Gundlach, B., & Blum, J. 2013, Icarus, 223, 479
Hanuš, J., Ďurech, J., Brož, M., et al. 2011, A&A, 530, A134
Hanuš, J., Ďurech, J., Brož, M., et al. 2013, A&A, 551, A67
Hanuš, J., Delbo', M., Ďurech, J., & Alí-Lagoa, V. 2015, Icarus, 256, 101
Hanuš, J., Ďurech, J., Oszkiewicz, D. A., et al. 2016, A&A, 586, A108
Hanuš, J., Delbo', M., Ďurech, J., & Alí-Lagoa, V. 2018, Icarus, 309, 297
Hapke, B. 1981, J. Geophys. Res., 86, 3039
Hapke, B. 1984, Icarus, 59, 41
Hapke, B. 1986, Icarus, 67, 264
Harris, A. W. 1998, Icarus, 131, 291
Harris, A. W., & Drube, L. 2016, ApJ, 832, 127
Harris, A. W., & Drube, L. 2020, ApJ, 901, 140
Harris, A. W., & Young, J. W. 1980, Icarus, 43, 20
Harris, A. W., Young, J. W., Dockweiler, T., et al. 1992, Icarus, 95, 115
Hayne, P. O., Bandfield, J. L., Siegler, M. A., et al. 2017, J. Geophys. Res. Planets, 122, 2371
Herald, D., Frappa, E., Gault, D., et al. 2019, Asteroid Occultations V3.0, NASA Planetary Data System
Herald, D., Gault, D., Anderson, R., et al. 2020, MNRAS, 499, 4570
Howell, S. B., Sobeck, C., Haas, M., et al. 2014, PASP, 126, 398
Jehin, E., Gillon, M., Queloz, D., et al. 2011, The Messenger, 145, 2
Kaasalainen, M., & Lamberg, L. 2006, Inverse Prob., 22, 749
Kaasalainen, M., & Ďurech J. 2020, ArXiv e-prints [arXiv:2005.09947]
Kaasalainen, M., Torppa, J., & Muinonen, K. 2001, Icarus, 153, 37
Keihm, S., Tosi, F., Kamp, L., et al. 2012, Icarus, 221, 395
Klinglesmith, Daniel A., I., Hendrickx, S., Kimber, C., & Madden, K. 2017, Minor Planet Bull., 44, 244
Lagerkvist, C. I., & Kamel, L. 1982, Moon Planets, 27, 463
Lagerkvist, C. I., Magnusson, P., Debehogne, H., et al. 1992, A&AS, 95, 461
Lagerros, J. S. V. 1996, A&A, 310, 1011
Lagerros, J. S. V. 1997, A&A, 325, 1226
Lagerros, J. S. V. 1998, A&A, 332, 1123
Lim, L. F., McConnochie, T. H., Bell, J. F., & Hayward, T. L. 2005, Icarus, 173, 385
Mainzer, A., Bauer, J., Grav, T., et al. 2011a, ApJ, 731, 53
Mainzer, A., Grav, T., Masiero, J., et al. 2011b, ApJ, 741, 90
Marchi, S., Paolicchi, P., & Richardson, D. C. 2012, MNRAS, 421, 2
Marciniak, A., Pilcher, F., Oszkiewicz, D., et al. 2015, Planet. Space Sci., 118, 256
Marciniak, A., Bartczak, P., Müller, T., et al. 2018, A&A, 610, A7
Marciniak, A., Alí-Lagoa, V., Müller, T. G., et al. 2019, A&A, 625, A139
Masiero, J. R., Mainzer, A. K., Grav, T., et al. 2011, ApJ, 741, 68
Morbidelli, A., Bottke, W. F., Nesvorný, D., & Levison, H. F. 2009, Icarus, 204, 558
Müller, T. G., Ďurech, J., Ishiguro, M., et al. 2017, A&A, 599, A103
Müller, T. G., Marciniak, A., Kiss, C., et al. 2018, Adv. Space Res., 62, 2326
Murdoch, N., Sánchez, P., Schwartz, S. R., & Miyamoto, H. 2015, Asteroids IV, Asteroid Surface Geophysics (Tucson: University of Arizona Press), 767
Neugebauer, G., Habing, H. J., van Duinen, R., et al. 1984, ApJ, 278, L1
Oey, J. 2009, Minor Planet Bull., 36, 4
Okada, T., Fukuhara, T., Tanaka, S., et al. 2020, Nature, 579, 518
Pál, A., Szakáts, R., Kiss, C., et al. 2020, ApJS, 247, 26
Pilcher, F. 2012, Minor Planet Bull., 39, 171
Pilcher, F. 2013, Minor Planet Bull., 40, 158
Pilcher, F. 2014, Minor Planet Bull., 41, 250
Ravaji, B., Alí-Lagoa, V., Delbo', M., & Wilkerson, J. W. 2019, J. Geophys. Res. Planets, 124, 3304
Ricker, G. R., Winn, J. N., Vanderspek, R., et al. 2015, J. Astron. Teles. Instrum. Syst., 1, 014003
Rozitis, B., Maclennan, E., & Emery, J. P. 2014, Nature, 512, 174
Rozitis, B., Green, S. F., MacLennan, E., & Emery, J. P. 2018, MNRAS, 477, 1782
Spencer, J. R., Lebofsky, L. A., & Sykes, M. V. 1989, Icarus, 78, 337
Stephens, R. D. 2009, Minor Planet Bull., 36, 157
Stephens, R. D. 2013, Minor Planet Bull., 40, 34
Stephens, R. D., Pilcher, F., Hamanowa, H., Hamanowa, H., & Ferrero, A. 2011, Minor Planet Bull., 38, 208
Szakáts, R., Müller, T., Alí-Lagoa, V., et al. 2020, A&A, 635, A54
Tedesco, E. F., Noah, P. V., Noah, M., & Price, S. D. 2004, NASA Planetary Data System, IRAS
Tholen, D. J. 1989, in Asteroids II, eds. R. P. Binzel, T. Gehrels, & M. S. Matthews (Tucson: University of Arizona Press), 1139
Usui, F., Kuroda, D., Müller, T. G., et al. 2011, PASJ, 63, 1117
Vokrouhlický, D., Bottke, W. F., Chesley, S. R., Scheeres, D. J., & Statler, T. S. 2015, Asteroids IV, eds. P. Michel, F. E. DeMeo, & W. F. Bottke (Tucson: University of Arizona Press), 509
Walsh, K. J., Jawin, E. R., Ballouz, R. L., et al. 2019, Nat. Geosci., 12, 242
Wang, X., Muinonen, K., & Wang, Y. 2015, Planet. Space Sci., 118, 242
Warner, B. D. 2006, Minor Planet Bull., 33, 85
Warner, B. D. 2007a, Minor Planet Bull., 34, 72
Warner, B. D. 2007b, Minor Planet Bull., 34, 104
Warner, B. D., & Harris, A. W. 2011, Icarus, 216, 610
Waszczak, A., Chang, C.-K., Ofek, E. O., et al. 2015, AJ, 150, 75
Weidenschilling, S. J., Chapman, C. R., Davis, D. R., et al. 1990, Icarus, 86, 402
Wright, E. L., Eisenhardt, P. R. M., Mainzer, A. K., et al. 2010, AJ, 140, 1868
Zappalà, V., Di Martino, M., Cellino, A., et al. 1989, Icarus, 82, 354

[1] Astronomical Observatory Institute, Faculty of Physics, A. Mickiewicz University, Słoneczna 36, 60-286 Poznań, Poland
e-mail: am@amu.edu.pl
[2] Astronomical Institute, Faculty of Mathematics and Physics, Charles University, V Holešovičkách 2, 180 00 Prague 8, Czech Republic
[3] Max-Planck-Institut für Extraterrestrische Physik (MPE), Giessenbachstrasse 1, 85748 Garching, Germany
[4] Mt. Suhora Observatory, Pedagogical University, Podchorążych 2, 30-084 Cracow, Poland
[5] Konkoly Observatory, Research Centre for Astronomy and Earth Sciences, Eötvös Loránd Research Network (ELKH), 1121 Budapest, Konkoly Thege Miklós út 15-17, Hungary
[6] MTA CSFK Lendület Near-Field Cosmology Research Group, Hungary
[7] ELTE Eötvös Loránd University, Institute of Physics, 1117, Pázmány Péter sétány 1/A, Budapest, Hungary
[8] Astronomy Department, Eötvös Loránd University, Pázmány P. s. 1/A, 1171 Budapest, Hungary
[9] Observatório Nacional, R. Gen. José Cristino, 77 - São Cristóvão, 20921-400, Rio de Janeiro - RJ, Brazil
[10] Geneva Observatory, 1290 Sauverny, Switzerland
[11] Oukaimeden Observatory, High Energy Physics and Astrophysics Laboratory, Cadi Ayyad University, Marrakech, Morocco
[12] Les Engarouines Observatory, 84570 Mallemort-du-Comtat, France
[13] Collonges Observatory, 74160 Collonges, France
[14] Flarestar Observatory Fl.5/B, George Tayar Street, San Gwann SGN 3160, Malta
[15] Stazione Astronomica, 28060 Sozzago (Novara), Italy
[16] Haute-Provence Observatory, St-Michel l'Observatoire, France

[17] Departamento de Sistema Solar, Instituto de Astrofísica de Andalucía (CSIC), Glorieta de la Astronomía s/n, 18008 Granada, Spain
[18] 11 rue du Puits Coellier, 37550 Saint-Avertin, France
[19] Observatoire du Bois de Bardon, 16110 Taponnat, France
[20] Association T60, Observatoire Midi-Pyrénées, 14, avenue Edouard Belin, 31400 Toulouse, France
[21] Aix Marseille Université, CNRS, CNES, Laboratoire d'Astrophysique de Marseille, Marseille, France
[22] Instituto de Astrofísica de Canarias, C/ Vía Lactea, s/n, 38205 La Laguna, Tenerife, Spain
[23] Gran Telescopio Canarias (GRANTECAN), Cuesta de San José s/n, 38712 Breña Baja, La Palma, Spain
[24] Faculty of Physics, Astronomy and Informatics, Nicolaus Copernicus University in Toruń, Poland
[25] School of Physical Sciences, The Open University, MK7 6AA, UK
[26] Space sciences, Technologies and Astrophysics Research Institute, Université de Liège, Allée du 6 Août 17, 4000 Liège, Belgium
[27] Institute of Physics, Jan Kochanowski University, ul. Uniwersytecka 7, 25-406 Kielce, Poland
[28] Chungbuk National University, 1, Chungdae-ro, Seowon-gu, Cheongju-si, Chungcheongbuk-do, Republic of Korea
[29] Korea Astronomy and Space Science Institute, 776 Daedeok-daero, Yuseong-gu, Daejeon 34055, Korea
[30] Institute of Physics, Faculty of Natural Sciences, University of P. J. Šafárik, Park Angelinum 9, 040 01 Košice, Slovakia
[31] Laboratory of Space Researches, Uzhhorod National University, Daleka st. 2a, 88000, Uzhhorod, Ukraine
[32] Dept. Astrofisica, Universidad de La Laguna, 38206 La Laguna, Tenerife, Spain
[33] Institute of Theoretical Physics and Astronomy, Vilnius University, Saulėtekio al. 3, 10257 Vilnius, Lithuania
[34] Organ Mesa Observatory, 4438 Organ Mesa Loop, Las Cruces, New Mexico 88011, USA
[35] Command Module Observatory, 121 W. Alameda Dr., Tempe, AZ 85282, USA
[36] Observatoire de Blauvac, 293 chemin de St Guillaume, 84570 St-Estève, France
[37] Departamento de Física, Ingeniería de Sistemas y Teoría de la Señal, Universidad de Alicante, Alicante, Spain
[38] Institut de Ciències del Cosmos, Universitat de Barcelona (IEEC-UB), Barcelona, Spain
[39] Lowell Observatory, 1400 West Mars Hill Road, Flagstaff, Arizona, 86001 USA
[40] Department of Physics, Adiyaman University, 02040 Adiyaman, Turkey
[41] European Southern Observatory, Karl-Schwarzschild-Strasse 2, 85748 Garching bei München, Germany
[42] Japan Spaceguard Association, Bisei Spaceguard Center, 1716-3, Okura, Bisei, Ibara, Okayama 714-1411, Japan
[43] Kepler Institute of Astronomy, University of Zielona Góra, Lubuska 2, 65-265 Zielona Góra, Poland

Appendix A: Chi-squared plots vs. thermal inertia

This section contains plots of $\chi^2_{\rm red}$ versus thermal inertia for various combinations of surface roughness and optimised size (Figures A.1 - A.16).

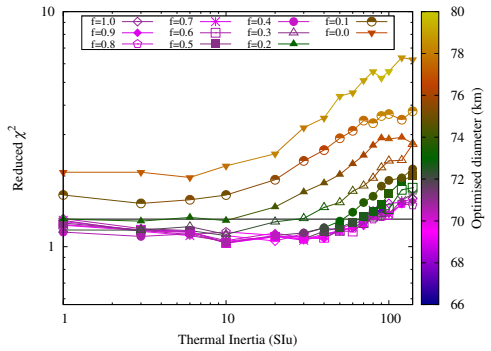


Fig. A.1: Reduced χ^2 values vs. thermal inertia for various combinations of surface roughness (symbol coded) and optimised diameters (colour coded) for asteroid (108) Hecuba.

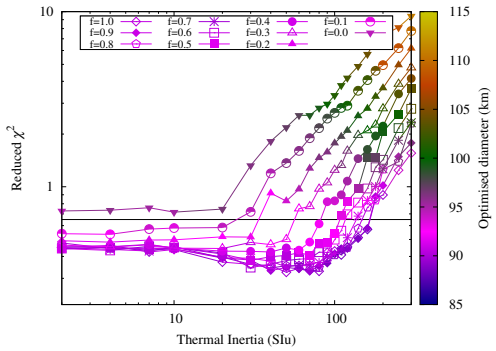


Fig. A.2: Reduced χ^2 values vs. thermal inertia for (202) Chryseis

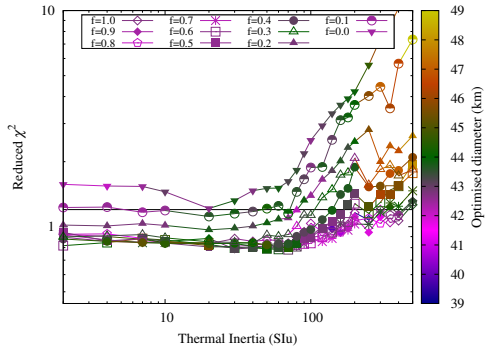


Fig. A.3: Reduced χ^2 values vs. thermal inertia for (219) Thusnelda

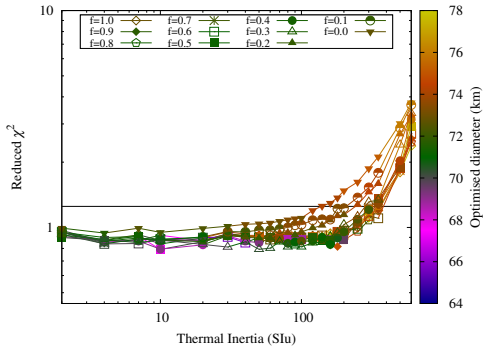


Fig. A.4: Reduced χ^2 values vs. thermal inertia for (223) Rosa

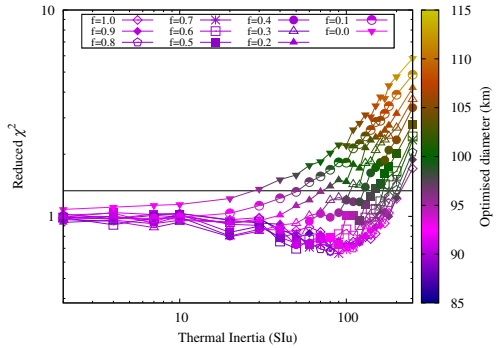


Fig. A.5: Reduced χ^2 values vs. thermal inertia for (362) Havnia

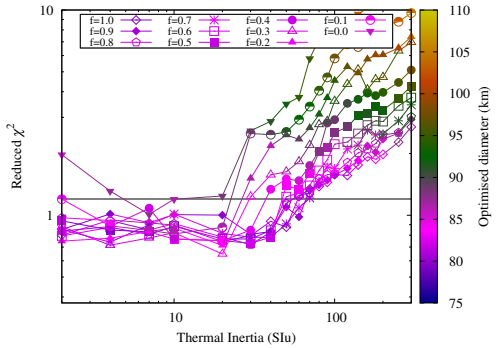


Fig. A.6: Reduced χ^2 values vs. thermal inertia for (478) Tergeste

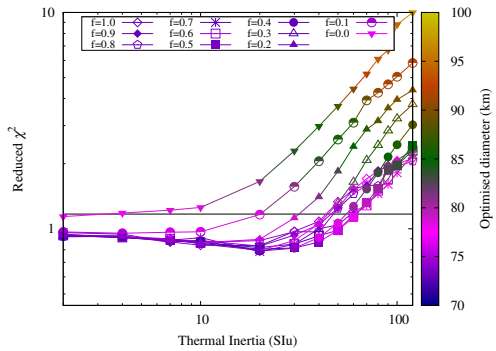


Fig. A.7: Reduced χ^2 values vs. thermal inertia for (483) Seppina

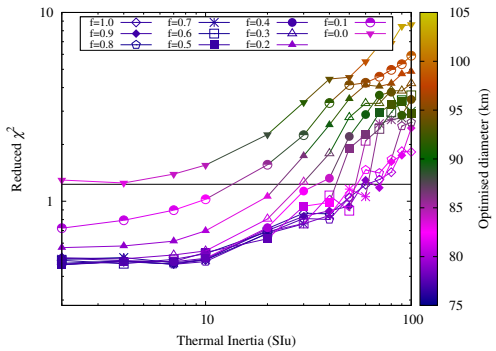


Fig. A.8: Reduced χ^2 values vs. thermal inertia for (501) Urhixidur

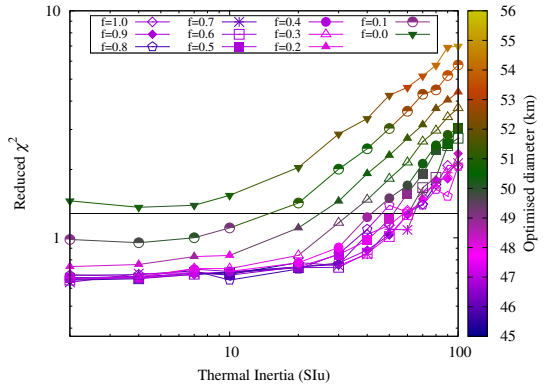


Fig. A.9: Reduced χ^2 values vs. thermal inertia for (537) Pauly

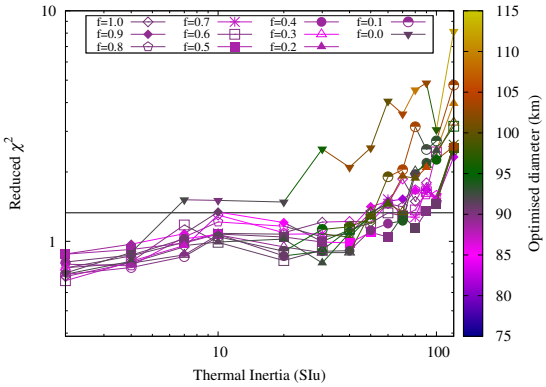


Fig. A.10: Reduced χ^2 values vs. thermal inertia for (552) Sigelinde

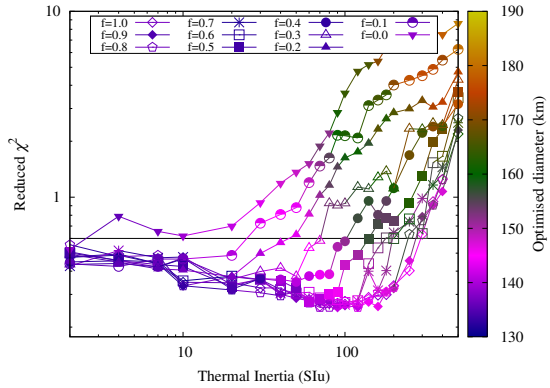


Fig. A.11: Reduced χ^2 values vs. thermal inertia for (618) Elfriede

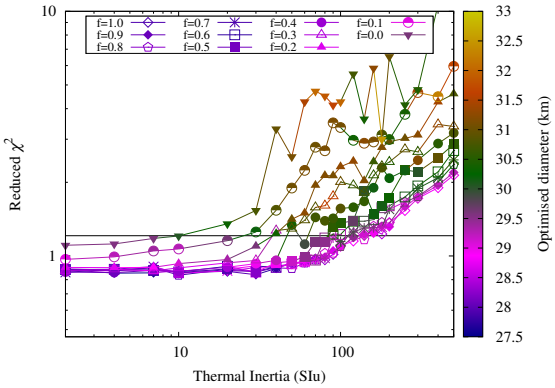


Fig. A.12: Reduced χ^2 values vs. thermal inertia for (666) Desdemona

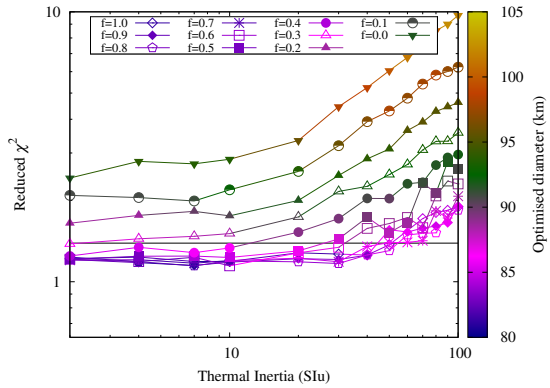


Fig. A.13: Reduced χ^2 values vs. thermal inertia for (667) Denise

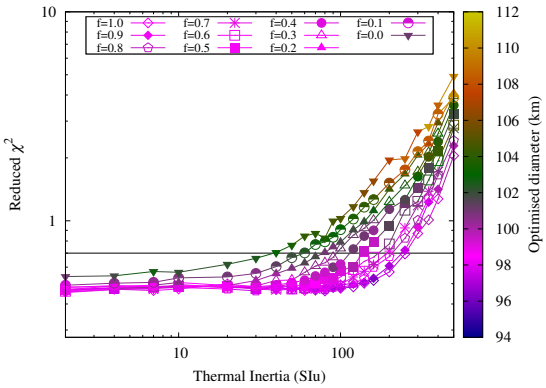


Fig. A.14: Reduced χ^2 values vs. thermal inertia for (780) Armenia

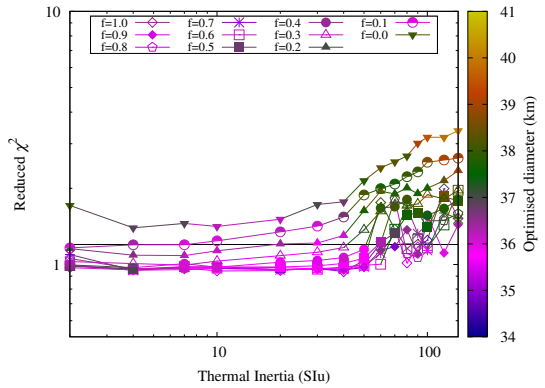


Fig. A.15: Reduced χ^2 values vs. thermal inertia for (923) Herluga

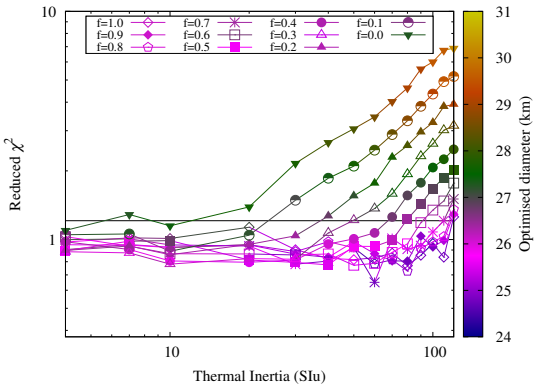


Fig. A.16: Reduced χ^2 values vs. thermal inertia for (995) Sternberga

Appendix B: Thermal light curves

Model fits to WISE thermal light curves (Figures B.1 - B.25).

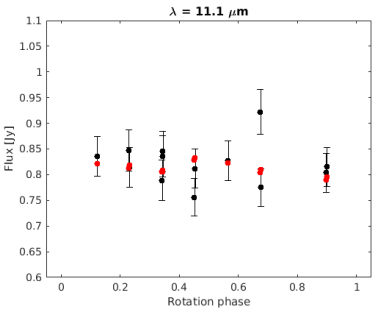


Fig. B.1: Infrared model fluxes (red circles) compared to measured fluxes in W3 band of WISE spacecraft (black circles) for asteroid (108) Hecuba.

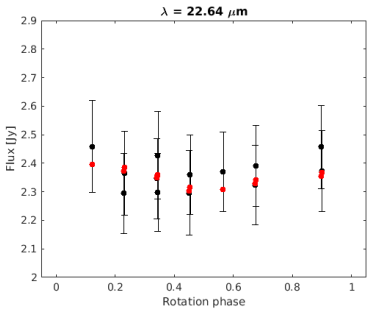


Fig. B.2: (108) Hecuba, thermal light curve in W4 band.

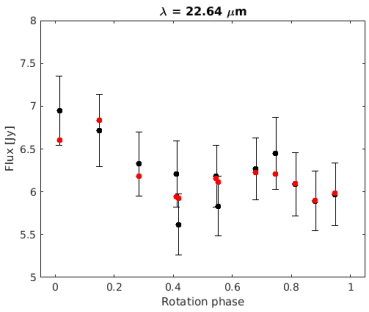


Fig. B.3: (202) Chryseis

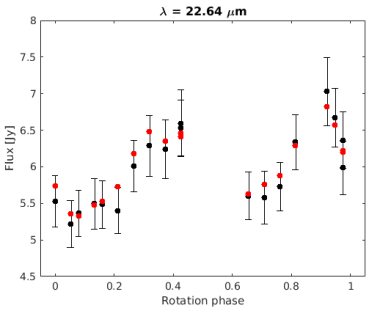


Fig. B.4: (219) Thusnelda

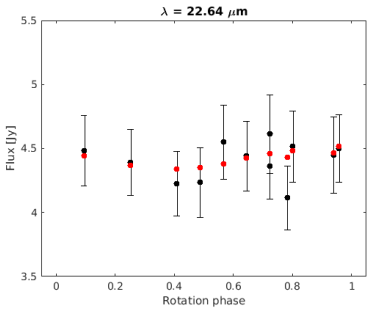


Fig. B.5: (223) Rosa

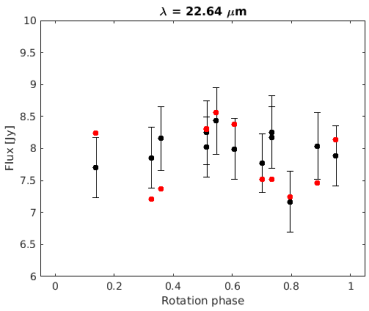


Fig. B.6: (362) Havnia

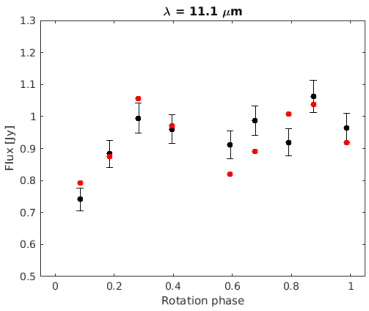


Fig. B.7: (478) Tergeste

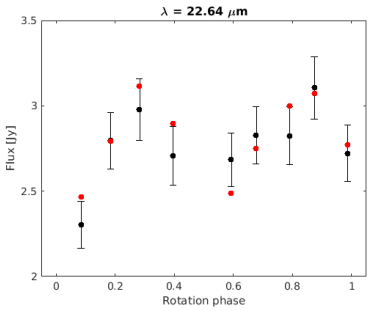


Fig. B.8: (478) Tergeste

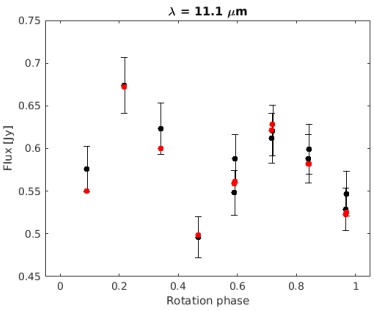


Fig. B.9: (483) Seppina

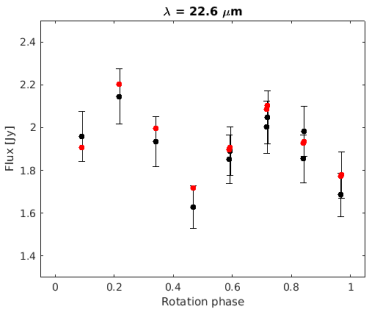


Fig. B.10: (483) Seppina

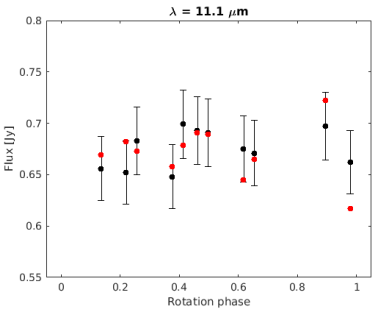


Fig. B.11: (501) Urhixidur

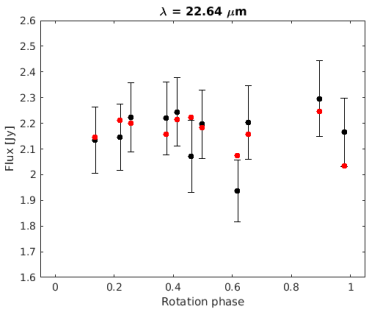


Fig. B.12: (501) Urhixidur

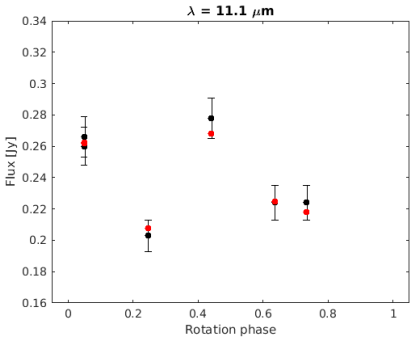


Fig. B.13: (537) Pauly

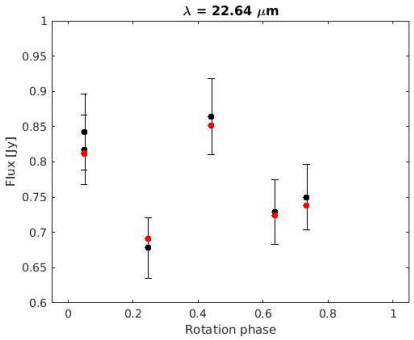


Fig. B.14: (537) Pauly

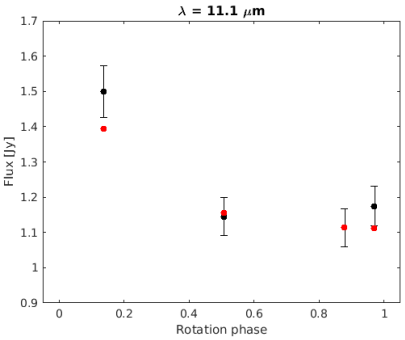


Fig. B.15: (552) Sigelinde

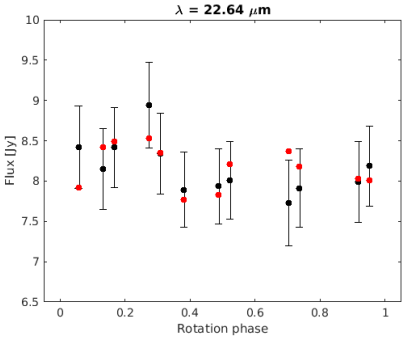


Fig. B.16: (618) Elfriede

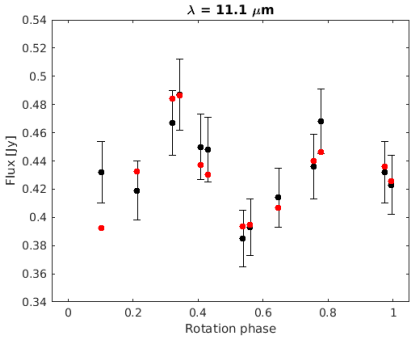


Fig. B.17: (666) Desdemona

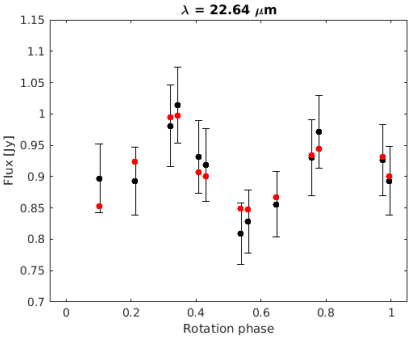


Fig. B.18: (666) Desdemona

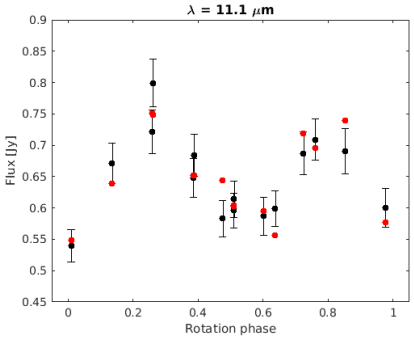


Fig. B.19: (667) Denise

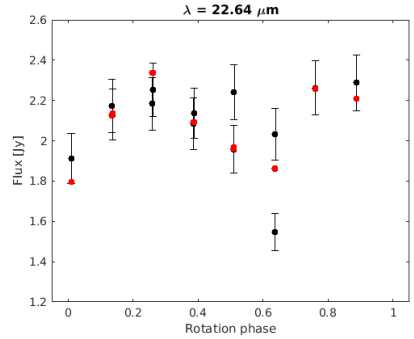


Fig. B.20: (667) Denise

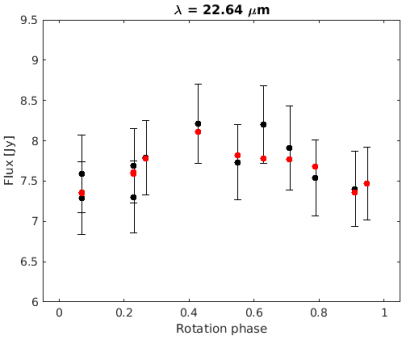


Fig. B.21: (780) Armenia

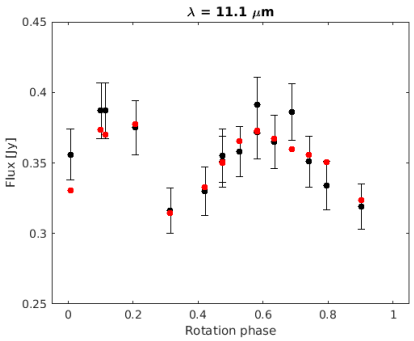


Fig. B.22: (923) Herluga

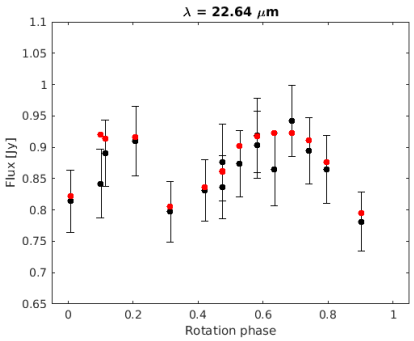


Fig. B.23: (923) Herluga

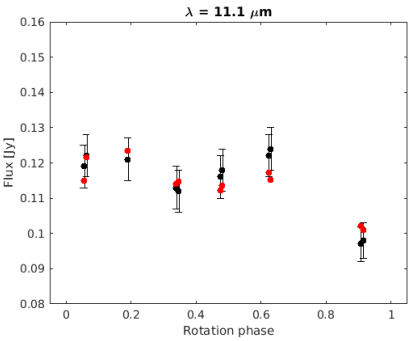


Fig. B.24: (995) Sternberga

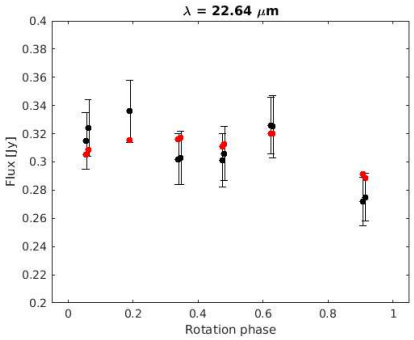


Fig. B.25: (995) Sternberga

Appendix C: Occultation fits

Instantaneous silhouettes of shape models from this work fitted to occultation timing chords.

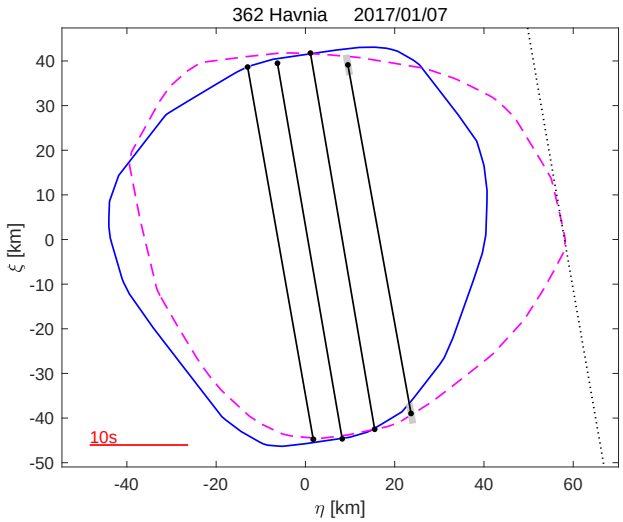


Fig. C.1: CITPM shape models of asteroid (362) Havnia fitted to a stellar occultation from 7. January 2017. In all the figures, north is up and west is right. The blue solid contour and the magenta dashed contour represent the model for pole 1 and pole 2, respectively. Black lines in those figures mark occultation shadow chords calculated from occultation timings, with timing uncertainties shown at the extremities of each chord. The scale in seconds is given for reference as a red line. Negative (no occultation) chords are marked with dotted lines, while visual observations (as opposed to video or photoelectric) are marked with dashed lines. See Table 3 for diameters of equivalent volume spheres.

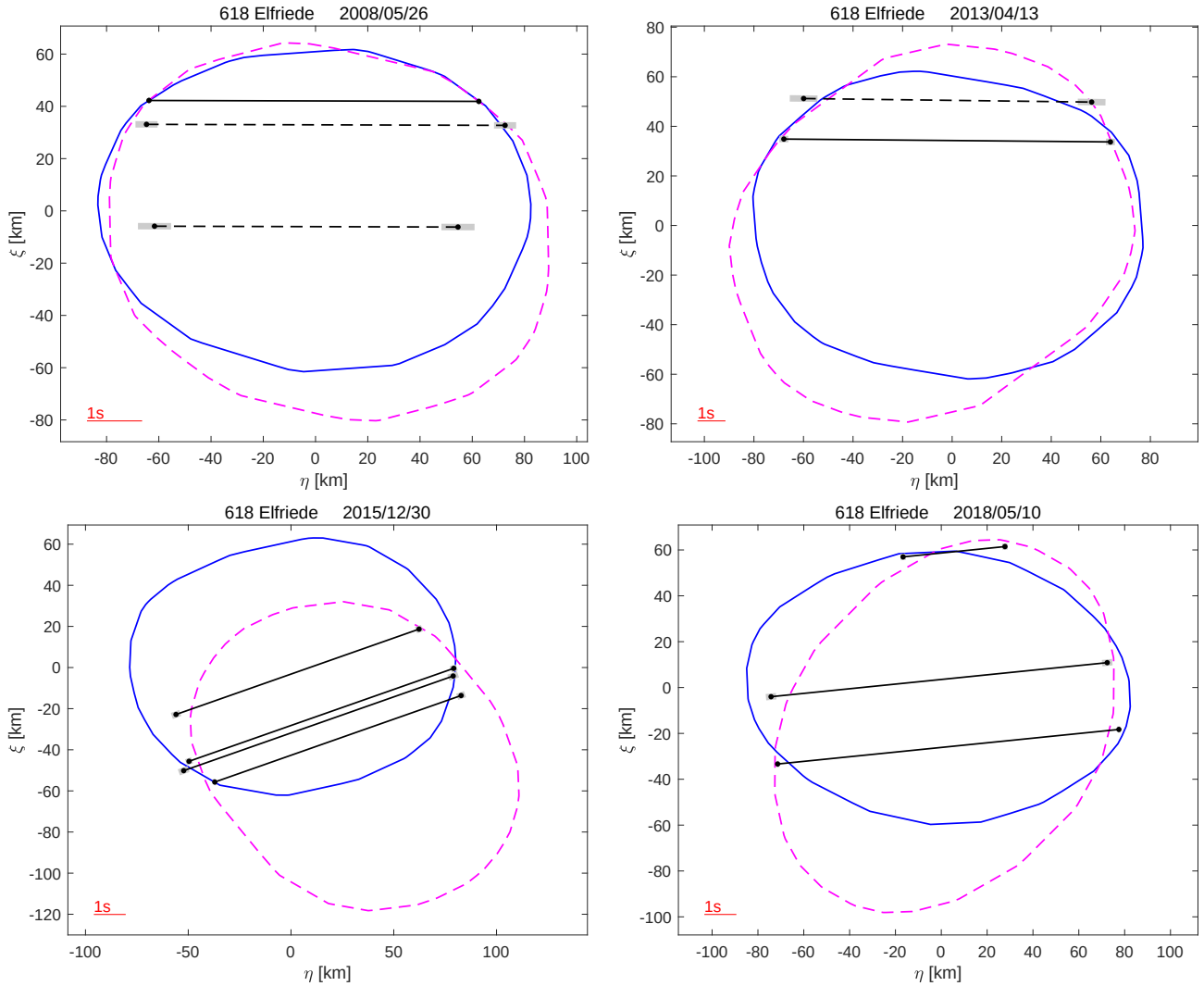


Fig. C.2: CITPM shape models of (618) Elfriede fitted to stellar occultations from 26 May 2008, 13 April 2013, 30 December 2015, and 10 May 2018. The visual, southernmost chord in the first event probably has an underestimated duration. See Table 3 for diameters of equivalent volume spheres. See caption of Fig. C.1 for description of the figure.

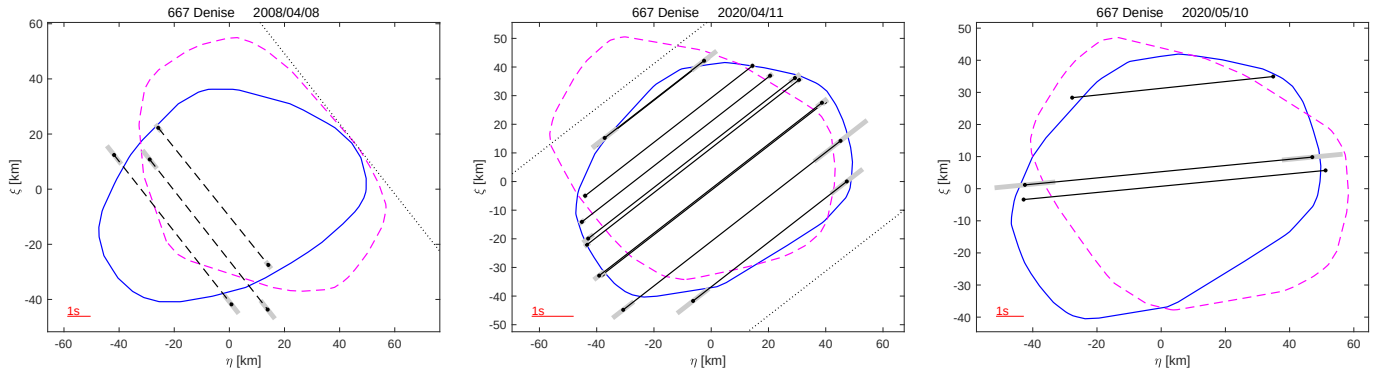


Fig. C.3: CITPM shape models of (667) Denise fitted to stellar occultations from 8 April 2008, 11 April 2020, and 10 May 2020. The pole 1 solution (blue contour) is clearly preferred over pole 2 (dashed magenta contour). See Table 3 for equivalent volume sphere diameter for the preferred pole solution. See caption of Fig. C.1 for description of the figure.

Appendix D: Observational details

Details of all light curve observations used for the modelling (Table D.1), and the list of stellar occultation observers and sites (Table D.2).

Table D.1: Details of all visible photometric observations: observing dates, number of light curves, ecliptic longitude of the target, sun-target-observer phase angle, observer's name (or paper citation in case of published data), and the observing site. Some data come from robotic telescopes, and so they have no observer specified. For data from the TESS spacecraft, the number of light curves denotes the number of days of continuous observations. CSSS stands for Center for Solar System Studies, PTF - Palomar Transient Factory, GMARS - Goat Mountain Astronomical Research Station, ESO - European Southern Observatory, SOAO - Sobaeksan Optical Astronomy Observatory, BOAO - Bohyunsan Optical Astronomy Observatory, LOAO - Lemonsan Optical Astronomy Observatory, OASI - Observatório Astronômico do Sertão de Itaparica, CTIO - Cerro Tololo Interamerican Observatory, ORM - Roque de los Muchachos Observatory.

Date	N_{lc}	λ [deg]	Phase angle [deg]	Observer	Site
(108) Hecuba					
2007 03 04 - 2007 03 09	5	126	11 - 12	Warner (2007a)	CSSS - Palmer Divide Station, USA
2011 11 30	1	68	2	T. Kundera	Suhora, Poland
2012 01 23 - 2012 03 05	7	61 - 66	15 - 17	Waszczak et al. (2015)	PTF, USA
2012 12 27 - 2013 02 26	8	140 - 149	2 - 14	Pilcher (2013)	Organ Mesa, USA
2014 04 20 - 2014 04 17	9	225 - 230	2 - 6	Pilcher (2014)	Organ Mesa, USA
2015 07 02	1	310	9	A. Marciniak	Teide, Spain
2015 08 05 - 2015 08 07	3	304	3 - 5	M. Żejmo	Adiyaman, Turkey
2015 08 10 - 2015 09 13	6	299 - 303	5 - 14	-	Montsec, Spain
2016 08 28 - 2017 01 08	7	7 - 19	7 - 16	A. Marciniak, R. Hirsch, K. Żukowski, M. Butkiewicz - Bąk	Borowiec, Poland
2017 11 03 - 2017 11 15	5	85 - 86	9 - 12	-	Montsec, Spain
2018 02 28 - 2018 03 02	2	75 - 76	18	J. Horbowicz, K. Żukowski	Borowiec, Poland
2019 01 19 - 2019 03 30	3	151 - 162	5 - 13	V. Kudak, V. Perig	Derenivka, Ukraine
2019 03 23	1	152	10	M. Żejmo	Suhora, Poland
2019 04 01	1	151	12	E. Pakštienė	Moletai, Lithuania
(202) Chryseis					
2011 01 19 - 2011 04 01	15	140 - 151	1 - 16	Stephens et al. (2011)	GMARS, USA; Organ Mesa, USA; Hamanowa, Japan; Bigmuskie, Italy
2013 07 31	1	311	1	-	Montsec, Spain
2014 09 05	1	24	12	P. Kankiewicz	Kielce, Poland
2014 09 16 - 2014 10 05	2	19 - 23	4 - 9	A. Marciniak	Borowiec, Poland
2014 10 10 - 2014 10 26	2	15 - 18	3 - 6	G. Stachowski, W. Ogłoza	Suhora, Poland
2014 10 31 - 2014 11 20	3	12 - 14	8 - 13	-	Montsec, Spain
2014 11 03	1	14	9	S. Urakawa	Bisei, Japan
2015 10 27 - 2016 01 28	6	102 - 112	9 - 20	R. Hirsch, I. Konstanciak, A. Marciniak, P. Kulczak	Borowiec, Poland
2015 11 08	1	112	19	P. Kankiewicz	Kielce, Poland
2016 01 10 - 2016 02 23	3	100 - 106	3 - 17	F. Pilcher	Organ Mesa, USA
2017 03 20 - 2017 05 28	6	202 - 213	4 - 14	F. Pilcher	Organ Mesa, USA
2017 03 24 - 2017 04 18	3	208 - 212	4 - 10	-	Montsec, Spain
2017 03 24	1	212	10	V. Kudak, V. Perig	Derenivka, Ukraine
2017 03 27	1	212	9	A. Marciniak	Borowiec, Poland
2018 07 19 - 2018 09 13	10	280 - 284	4 - 16	-	Montsec, Spain
2019 08 23 - 2019 09 18	5	350 - 355	3 - 7	S. Fauvaud	Le Bois de Bardon, France
2019 08 25 - 2019 10 14	3	346 - 355	4 - 10	W. Ogłoza	Adiyaman, Turkey
2019 09 18 - 2019 09 20	3	350	3	-	Montsec, Spain
2019 10 05	1	347	7	K. Kamiński	Winer, USA
2019 10 07	1	346	8	V. Kudak, V. Perig	Derenivka, Ukraine
2019 10 14	1	346	10	R. Szakáts	Piszkéstető, Hungary
(219) Thusnelda					
1981 08 21 - 1981 09 27	7	340 - 347	8 - 14	Harris et al. (1992)	Table Mountain, USA
1981 09 02 - 1981 09 06	5	344 - 345	8 - 9	Lagerkvist & Kamel (1982)	ESO, Chile
2013 05 25 - 2013 06 30	14	236 - 238	6 - 21	-	Montsec, Spain
2013 05 27 - 2013 06 26	4	236 - 238	7 - 19	F. Pilcher	Organ Mesa, USA
2014 10 10 - 2014 12 24	26	81 - 95	7 - 26	Marciniak et al. (2015)	Suhora, Poland; Borowiec, Poland, Organ Mesa, USA; Winer, USA; Montsec, Spain; Bisei, Japan
2015 01 07	1	81	12	F. Pilcher	Organ Mesa, USA
2016 02 04 - 2016 03 06	5	181 - 186	5 - 15	-	Montsec, Spain
2016 02 08 - 2016 02 27	4	183 - 186	9 - 14	K. Kamiński	Winer, USA
2016 02 27 - 2016 03 31	4	175 - 183	2 - 9	F. Pilcher	Organ Mesa, USA
2016 04 02 - 2016 04 21	3	174 - 171	7 - 14	P. Kulczak, K. Żukowski, R. Hirsch	Borowiec, Poland
2017 05 26 - 2016 05 27	2	311	27	M.-J. Kim	SOAO, South Korea
2017 06 23	1	314	22	R. Szakáts	Piszkéstető, Hungary
2017 07 03 - 2017 07 04	2	314	18 - 19	R. Duffard	La Sagra, Spain
2017 07 13 - 2017 08 16	4	306 - 313	12 - 15	S. Brincat	Flarestar, Malta
2017 07 13 - 2017 09 08	10	304 - 313	15 - 23	-	Montsec, Spain
2018 11 15 - 2019 02 08	2	125 - 135	8 - 22	V. Kudak, V. Perig	Derenivka, Ukraine
2018 12 10 - 2019 02 14	14	124 - 137	7 - 18	-	Montsec, Spain
2019 01 04 - 2019 01 31	6	127 - 134	6 - 12	F. Pilcher	Organ Mesa, USA
2019 01 30 - 2019 02 06	2	126 - 127	6 - 7	A. Marciniak	Borowiec, Poland

Date	N_{lc}	λ [deg]	Phase angle [deg]	Observer	Site
(223) Rosa					
2007 03 25 - 2007 04 14	4	166 - 169	5 - 12	Warner (2007b)	CSSS, USA
2011 12 30 - 2012 02 10	8	121 - 129	2 - 10	Pilcher (2012)	Organ Mesa, USA
2015 09 07 - 2015 10 09	3	344 - 350	1 - 10	S. Fauvaud	Le Bois de Bardon, France
2015 09 01 - 2015 09 03	2	347	4	S. Fauvaud, M. Fauvaud, F. Richard	Pic du Midi, France
2015 11 22	1	344	18	D. Oszkiewicz	Lowell, USA
2016 11 01 - 2016 12 18	6	72 - 82	1 - 14	-	Montsec, Spain
2016 12 28	1	72	9	J. Horbowicz	Borowiec, Poland
2018 02 16 - 2018 02 25	2	184 - 185	9 - 12	R. Hirsch	Borowiec, Poland
2018 03 23	1	179	2	V. Kudak	Derenivka, Ukraine
2018 04 12 - 2018 04 19	8	174 - 175	9 - 11	-	Kepler Space Observatory
2019 05 15 - 2019 06 01	5	257 - 250	2 - 7	-	Montsec, Spain
2019 05 23	1	259	5	K. Kamiński	Winer, USA
2019 07 11	1	250	13	M. Ferrais, E. Jehin	TRAPPIST-South, Chile
2020 07 19 - 2020 10 19	9	312 - 322	1 - 16	M. Ferrais, E. Jehin	TRAPPIST-North, Morocco
2020 08 23 - 2020 08 25	4	316	4 - 5	F. Monteiro, M. Evangelista-Santana, E. Rondón, P. Arcoverde, J. Michimani-Garcia, D. Lazzaro, T. Rodrigues	OASI, Itacuruba, Brasil
2020 10 18 - 2020 10 19	2	313	16	M. Ferrais, E. Jehin	TRAPPIST-South, Chile
(362) Havnia					
1978 12 04	1	63	5	Harris & Young (1980)	Table Mountain, USA
2006 06 05 - 2006 08 26	5	299 - 312	9 - 19	-	SuperWASP
2009 04 06 - 2009 04 20	6	180 - 186	5 - 11	Stephens (2009)	Rancho Cucamonga, USA
2015 10 28 - 2015 12 10	3	24 - 30	2 - 19	M. Butkiewicz - Bąk, A. Marciniak, P. Kulczak	Borowiec, Poland
2015 11 29 - 2015 12 01	2	24	16	-	Montsec, Spain
2016 12 22 - 2017 03 03	4	152 - 160	6 - 21	J. Horbowicz, A. Marciniak, K. Żukowski, M. Butkiewicz - Bąk	Borowiec, Poland
2017 01 19	1	161	15	V. Kudak, V. Perig	Derenivka, Ukraine
2017 01 25 - 2017 01 31	7	159 - 160	11 - 13	T. Polakis, B. Skiff	Command Module, USA
2018 07 26	1	252	17	A. Marciniak	CTIO, Chile
2019 08 29 - 2019 09 19	2	17 - 20	8 - 16	S. Fauvaud	Le Bois de Bardon, France
2019 09 04	1	19	14	V. Kudak, V. Perig	Derenivka, Ukraine
2019 09 21	1	16	7	J. Skrzypek	Borowiec, Poland
2019 09 28 - 2019 10 15	2	11 - 15	4 - 5	W. Ogłoza	Adiyaman, Turkey
2019 10 17 - 2020 01 10	2	10 - 14	6 - 13	R. Szakáts	Piszkéstető, Hungary
(483) Seppina					
1986 07 11 - 1986 07 27	6	268 - 270	9 - 12	Zappalà et al. (1989)	ESO, La Silla, Chile
2005 06 25 - 2005 07 11	2	264 - 266	8 - 10	F. Manzini	Sozzago, Italy
2005 07 04	1	265	9	G. Farroni, P. Pinel	Saint-Avertin, France
2005 07 10 - 2005 07 30	4	262 - 264	10 - 13	R. Roy	Blauvac, France
2005 07 12	1	264	11	L. Bernasconi	Engarouines, France
2006 08 21	1	348	6	L. Brunetto	Le Florian, France
2013 10 08 - 2013 12 23	4	25 - 34	5 - 16	K. Sobkowiak, D. Oszkiewicz, A. Marciniak	Borowiec, Poland
2013 12 16 - 2013 12 17	4	25 - 33	5 - 15	F. Pilcher	Organ Mesa, USA
2015 01 20 - 2015 03 22	3	96 - 97	9 - 16	K. Kamiński	Winer, USA
2015 02 12 - 2015 03 18	2	94 - 95	13 - 16	A. Marciniak, J. Horbowicz, M. Figas	Borowiec, Poland
2016 01 03 - 2016 04 01	5	155 - 167	5 - 14	P. Kulczak, A. Marciniak, R. Hirsch, M. Butkiewicz - Bąk	Borowiec, Poland
2017 04 01 - 2017 05 29	9	214 - 224	5 - 10	R. Hirsch, K. Żukowski, J. Horbowicz, A. Marciniak, J. Skrzypek	Borowiec, Poland
2018 07 19 - 2018 08 15	14	287 - 291	7 - 12	-	Montsec, Spain
(501) Urhixidur					
1990 08 22 - 1990 08 29	6	327 - 329	6 - 7	Lagerkvist et al. (1992)	ESO, La Silla, Chile
2013 09 06 - 2013 12 30	5	18 - 28	6 - 20	R. Hirsch, T. Santana-Ros, D. Oszkiewicz, A. Marciniak	Borowiec, Poland
2014 10 29 - 2015 03 17	6	104 - 117	8 - 18	R. Hirsch, A. Marciniak, I. Konstanciak, J. Horbowicz	Borowiec, Poland
2015 01 21 - 2015 04 29	2	109 - 111	8 - 16	K. Kamiński	Winer, USA
2015 03 22 - 2015 03 23	2	105	17	W. Ogłoza, A. Marciniak, V. Kudak	Suhora, Poland
2016 02 06 - 2016 04 29	4	163 - 176	2 - 14	A. Marciniak, R. Hirsch	Borowiec, Poland
2016 02 13 - 2016 03 01	4	172 - 175	3 - 8	K. Kamiński	Winer, USA
2017 02 08 - 2017 03 09	2	231 - 233	15 - 16	A. Marciniak	CTIO, Chile
2017 05 04	1	227	7	F. Monteiro	OASI, Brasil
2018 08 04 - 2018 08 22	18	312 - 315	8 - 9	Pál et al. (2020)	TESS Spacecraft
2018 08 14	1	313	8	A. Marciniak	CTIO, Chile
2018 09 14 - 2018 09 15	2	309	15	F. Monteiro, E. Rondón, M. Evangelista-Santana, P. Arcoverde, D. Lazzaro, T. Rodrigues	OASI, Brasil
2019 08 12 - 2019 08 19	4	58 - 59	21	W. Ogłoza	Adiyaman, Turkey
2019 10 11 - 2019 12 15	2	52 - 64	12 - 15	R. Szakáts, V. Kecskeméthy	Piszkéstető, Hungary
2019 10 12 - 2019 10 15	2	64	14 - 15	J. Skrzypek, M. Pawłowski	Borowiec, Poland
(537) Pauly					
1984 05 10	1	211	8	Weidenschilling et al. (1990)	Kitt Peak, USA
1985 09 08 - 1985 09 12	4	354 - 355	6	Barucci et al. (1992)	ESO, Chile
1989 04 16	1	182	7	Weidenschilling et al. (1990)	Kitt Peak, USA
2016 02 24 - 2016 03 10	4	202 - 204	10 - 13	K. Kamiński	Winer, USA
2016 03 18 - 2016 05 09	4	191 - 201	8 - 12	M. Butkiewicz - Bąk, A. Marciniak, P. Kulczak	Borowiec, Poland
2017 08 03 - 2017 09 24	9	311 - 316	2 - 19	-	Montsec, Spain
2018 10 09 - 2018 11 29	5	65 - 73	4 - 15	K. Żukowski, A. Marciniak, M. K. Kamińska, J. Krajewski, M. Pawłowski	Borowiec, Poland
2018 11 26 - 2018 12 10	16	62 - 66	4 - 6	Pál et al. (2020)	TESS Spacecraft
2019 11 24 - 2019 12 17	3	126 - 128	10 - 14	W. Ogłoza	Adiyaman, Turkey
2019 11 27	1	128	14	M.-J. Kim, D.-H. Kim	SOAO, South Korea
2019 12 05	1	127	12	A. Marciniak	Borowiec, Poland
2020 01 15	1	122	2	V. Kudak, V. Perig	Derenivka, Ukraine

Date	N_{lc}	λ [deg]	Phase angle [deg]	Observer	Site
(552) Sigelinde					
2008 04 11 - 2008 05 03	8	245 - 247	7 - 14	Oey (2009)	Leura, Australia
2010 08 13 - 2011 01 26	11	42 - 52	2 - 18	Waszczak et al. (2015)	Palomar Transient Factory, USA
2015 08 25 - 2015 10 02	5	6 - 12	3 - 12	A. Marciniak, R. Hirsch, P. Kulczak	Borowiec, Poland
2016 11 20 - 2016 12 05	2	74 - 76	1 - 5	K. Żukowski, R. Hirsch	Borowiec, Poland
2017 01 15	1	67	12	S. Geier	ORM, Spain
2017 01 25	1	67	14	M.-J. Kim, D.-H. Kim	SOAO, South Korea
2017 02 08	1	67	16	A. Marciniak	CTIO, Chile
2017 02 10 - 2017 02 11	2	67	16	M.-J. Kim, D.-H. Kim	BOAO, South Korea
2018 02 23 - 2018 04 09	3	132 - 136	6 - 17	A. Marciniak, R. Hirsch, K. Żukowski	Borowiec, Poland
2018 03 14 - 2018 03 16	2	133	12	M.-J. Kim, D.-H. Kim	BOAO, South Korea
2018 03 19	1	133	13	K. Kamiński	Winer, USA
2019 04 26 - 2019 04 29	4	224 - 225	3 - 4	K. Kamiński	Winer, USA
2019 05 11	1	222	4	-	Montsec, Spain
2019 04 26 - 2019 05 19	23	220 - 225	3 - 7	Pál et al. (2020)	TESS Spacecraft
(618) Elfriede					
1984 05 12	1	236	6	Weidenschilling et al. (1990)	Kitt Peak, USA
1989 04 16 - 1989 04 17	2	183	9	Weidenschilling et al. (1990)	Kitt Peak, USA
2004 12 03 - 2004 12 11	6	125	12 - 14	L. Bernasconi	Engarouines, France
2006 05 12 - 2006 06 02	7	175 - 176	15 - 17	Warner (2006)	Palmer Divide, USA
2014 10 01 - 2014 12 09	12	4 - 10	8 - 18	-	Montsec, Spain
2015 10 10 - 2016 01 27	5	86 - 98	4 - 18	-	Montsec, Spain
2016 01 22	1	87	10	A. Marciniak	Borowiec, Poland
2016 12 29 - 2017 04 09	4	150 - 163	8 - 15	J. Horbowicz, K. Żukowski	Borowiec, Poland
2017 01 25	1	162	10	M.-J. Kim, D.-H. Kim	SOAO, South Korea
2017 02 04 - 2017 03 14	2	153 - 160	8	W. Ogłoza, M. Żejmo	Suhora, Poland
2017 02 22 - 2017 02 25	4	157	5	T. Polakis, B. Skiff	Command Module, USA
2017 03 02 - 2017 03 17	9	153 - 156	5 - 8	Klinglesmith et al. (2017)	Socorro, USA
2018 02 27 - 2018 05 09	5	226 - 232	7 - 17	K. Żukowski, J. Horbowicz, A. Marciniak, J. Skrzypek	Borowiec, Poland
2019 07 22 - 2019 07 26	5	306	2 - 3	W. Ogłoza	Adiyaman, Turkey
(666) Desdemona					
2013 10 02 - 2014 02 14	8	82 - 95	9 - 29	Marciniak et al. (2015)	Borowiec, Poland; Winer, USA
2014 12 31 - 2015 03 14	15	192 - 196	5 - 19	-	Montsec, Spain
2015 02 11 - 2015 03 31	2	186 - 197	6 - 15	K. Kamiński	Winer, USA
2015 03 18	1	191	5	M. Figas	Borowiec, Poland
2016 04 16	2	264	16	S. Geier	Kitt Peak, USA
2016 04 29	1	264	13	S. Geier	ORM, Spain
2016 05 01	1	263	13	-	Montsec, Spain
2016 06 30 - 2016 07 05	4	251 - 252	10 - 11	R. Duffard, N. Morales	La Sagra, Spain
2016 07 23	1	249	17	A. Marciniak	Teide, Spain
2017 09 16 - 2017 09 22	7	57 - 58	27 - 25	T. Polakis, B. Skiff	Tempe, USA
2017 09 18 - 2018 01 08	5	48 - 58	5 - 25	J. Horbowicz, K. Żukowski, R. Hirsch	Borowiec, Poland
2019 01 07	1	184	19	R. Duffard, N. Morales	La Sagra, Spain
2019 02 01 - 2019 04 07	6	172 - 184	3 - 15	-	Montsec, Spain
2019 02 07	1	184	14	Cs. Kalup	Piszkéstető, Hungary
2019 04 01 - 2019 04 03	2	173	6 - 7	M. Pawłowski, J. Krajewski	Borowiec, Poland
(667) Denise					
2014 03 28 - 2014 05 19	5	166 - 169	8 - 19	R. Hirsch, K. Sobkowiak, I. Konstanciak, P. Trela	Borowiec, Poland
2015 03 23 - 2015 03 24	2	252	15	W. Ogłoza, A. Marciniak. V. Kudak	Suhora, Poland
2015 04 21 - 2015 04 23	2	250 - 251	12	J. Horbowicz, A. Marciniak	Borowiec, Poland
2015 05 31	1	243	9	K. Kamiński	Winer, USA
2015 06 27	1	238	12	A. Marciniak	Teide, Spain
2016 07 23 - 2016 07 26	3	298	5 - 6	-	Montsec, Spain
2016 07 30 - 2016 08 20	4	293 - 297	6 - 10	R. Szakáts, E. Verebélyi	Piszkéstető, Hungary
2016 08 26	1	293	11	S. Geier	ORM, Spain
2016 08 31	1	292	12	K. Żukowski	Borowiec, Poland
2017 08 07	1	359	12	W. Ogłoza	Suhora, Poland
2017 08 27	1	357	8	A. Marciniak	Teide, Spain
2017 08 31 - 2017 09 18	8	352 - 356	4 - 6	-	Montsec, Spain
2018 11 23 - 2019 01 27	9	96 - 108	15 - 18	-	Montsec, Spain
2019 02 18	1	94	19	M. K. Kamińska	Borowiec, Poland

Date	N_{lc}	λ [deg]	Phase angle [deg]	Observer	Site
(780) Armenia					
2004 06 07 - 2004 07 15	3	256 - 263	8 - 13	J.-G. Bosch	Collonges, France
2009 05 02 - 2009 06 02	15	217 - 223	8 - 12	Benishek & Pilcher (2009)	Organ Mesa, USA; Belgrade, Serbia
2010 07 20 - 2010 08 31	2	298 - 306	5 - 13	R. Roy	Blauvac, France
2014 02 25 - 2014 05 31	8	182 - 194	11 - 15	J. Horbowicz, A. Marciniak, I. Konstanciak, D. Oszkiewicz, T. Santana - Ros, K. Sobkowiak	Borowiec, Poland
2015 04 16 - 2015 05 30	4	265 - 268	9 - 16	P. Kulczak, A. Marciniak	Borowiec, Poland
2015 05 21 - 2015 06 22	7	260 - 266	8 - 11	K. Kamiński	Winer, USA
2015 06 17 - 2015 07 06	11	257 - 261	8 - 11	-	Montsec, Spain
2016 08 02	1	355	8	A. Marciniak	CTIO, Chile
2016 10 08 - 2016 10 15	2	346	11 - 13	-	Montsec, Spain
2016 10 10 - 2016 11 08	12	345 - 346	11 - 18	B. Skiff	Lowell, USA
2016 12 04 - 2016 12 05	2	348	20	T. Polakis, B. Skiff	Command Module, USA
2017 12 15 - 2017 01 21	3	84 - 91	8 - 12	F. Monteiro, H. Medeiros, E. Rondón, P. Arcoverde, D. Lazzaro, T. Rodrigues	OASI, Brasil
2017 12 17 - 2018 02 13	3	83 - 90	7 - 16	M.-J. Kim, D.-H. Kim	SOAO, South Korea
2018 01 03 - 2018 01 05	2	86 - 87	8 - 9	M.-J. Kim, D.-H. Kim	LOAO, USA
2018 01 24 - 2018 03 27	2	84 - 88	13 - 18	K. Kamiński	Winer, USA
2018 02 08 - 2018 02 16	2	83	16 - 17	M. Butkiewicz - Bąk, R. Hirsch	Borowiec, Poland
2018 12 04 - 2019 01 06	3	163 - 165	14 - 17	M.-J. Kim, D-H. Kim	SOAO, South Korea
2019 01 19 - 2019 03 30	6	152 - 164	2 - 12	R. Hirsch, J. Krajewski, A. Marciniak, K. Żukowski, J. Skrzypek	Borowiec, Poland
2019 02 22	1	159	2	V. Kudak, V. Perig	Derenivka, Ukraine
(923) Herluga					
2008 10 07 - 2008 11 29	8	39 - 49	8 - 16	Brinsfield (2009)	Via Capote, USA
2012 10 19 - 2012 10 31	2	354 - 355	14 - 19	R. Hirsch, J. Nadolny	Borowiec, Poland
2014 03 14 - 2014 04 18	7	149 - 152	9 - 18	-	Montsec, Spain
2015 03 17 - 2015 03 27	6	227 - 238	7 - 16	-	Montsec, Spain
2015 04 18 - 2015 06 22	3	223 - 235	4 - 14	K. Kamiński	Winer, USA
2016 07 25 - 2016 09 10	12	330 - 320	8 - 14	Marciniak et al. (2018)	Montsec, Spain; ORM, Spain; Borowiec, Poland
2018 03 18 - 2018 03 30	3	126	18 - 20	K. Kamiński	Winer, USA
2019 03 30 - 2019 04 01	3	220	9 - 10	R. Szakáts	Piszkéstető, Hungary
2019 04 26 - 2019 05 11	7	211 - 215	2 - 7	-	Montsec, Spain
(995) Sternberga					
1989 01 07 - 1989 01 12	4	124 - 126	8 - 9	Barucci et al. (1992)	ESO, La Silla, Chile
2007 03 21 - 2007 03 24	2	211 - 212	9 - 10	-	Super WASP
2012 06 30 - 2012 07 15	10	292 - 292	9 - 11	Stephens (2013)	Racho Cucamonga, USA
2013 11 13 - 2014 02 04	4	79 - 93	7 - 18	A. Marciniak, I. Konstanciak, P. Trela, J. Horbowicz, R. Hirsch	Borowiec, Poland
2013 12 06 - 2013 12 15	5	87 - 89	5 - 7	F. Pilcher	Organ Mesa, USA
2014 01 02 - 2014 02 21	4	80 - 82	9 - 20	K. Kamiński	Winer, USA
2015 01 01 - 2015 03 16	15	169 - 178	5 - 18	-	Montsec, Spain
2015 02 11	1	177	11	K. Kamiński	Winer, USA
2015 02 25	1	174	7	F. Pilcher	Organ Mesa, USA
2015 03 23	1	168	7	R. Hirsch	Borowiec, Poland
2016 05 04 - 2016 07 10	24	252 - 265	5 - 15	Marciniak et al. (2018)	Lowell, USA; Teide, Spain; Derenivka, Ukraine; Command Module, USA; La Sagra, Spain; Montsec, Spain; Bardon, France
2017 10 24	1	66	14	V. Kudak, V. Perig	Derenivka, Ukraine
2017 12 07 - 2018 02 06	3	53 - 56	8 - 22	M. Butkiewicz - Bąk, R. Hirsch, J. Skrzypek	Borowiec, Poland

(362) Havnia, 2017-01-07	
P. Maley	Gila Bend, AZ
C. Wiesenborn	Boulder City, NV
W. Thomas	Florence, AZ
T. George	Scottsdale, AZ
(618) Elfriede, 2008-05-26	
D. Breadsell	Toowoomba, Qld, AU
J. Bradshaw	Samford, Qld, AU
P. Anderson	Range Observatory, Qld, AU
(618) Elfriede, 2013-04-13	
D. Herald	Murrumbateman, NSW
J. Drummond	Patutahi, Gisborne, NZ
(618) Elfriede, 2015-12-30	
J. Rovira	ES
R. Naves	ES
C. Perello, A. Selva	ES
C. Schnabel	ES
(618) Elfriede, 2018-05-10	
J. Broughton	Woodburn, NSW, AU
J. Broughton	Grafton, NSW, AU
J. Broughton	Mullaway, NSW, AU
(667) Denise, 2008-04-08	
R. Nugent	Pontotoc, TX
G. Nason	Tobermory, ONT, CA
M. McCants	Kingsland, TX
P. Maley, D. Weber	Horseshoe Bay, TX
(667) Denise, 2020-04-11	
S. Meister	CH
A. Schweizer	CH
C. Ellington	DE
S. Sposetti	CH
A. Manna	CH
A. Ossola	CH
O. Schreurs	BE
M. Bigi	IT
P. Baruffetti	IT
F. Van Den Abbeel	BE
J. Bourgeois	BE
R. Boninsegna	BE
(667) Denise, 2020-05-10	
K. Hanna	MT
K. Green	CT
R. Kamin	PA
S. Conard	MD
K. Getrost	OH
A. Scheck	MD
A. Caroglanian	MD
J. Massura	IN
J. Harris	VA
C. Anderson, K. Thomason	ID
M. Wasiuta, B. Billard	VA
B. Billard	VA

Table D.2: List of stellar occultation observers and locations of the observing sites.

Appendix E: Visible light curves

Composite light curves in the visible, with the new data of target asteroids (Figures E.1 - E.66).

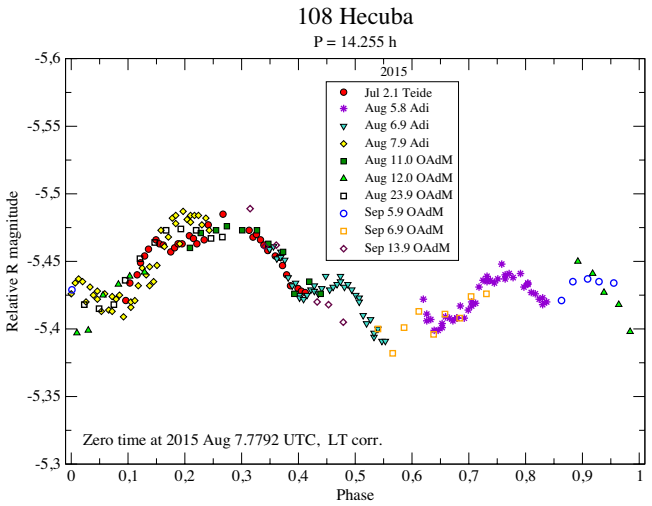


Fig. E.1: Composite light curve of (108) Hecuba from the year 2015.

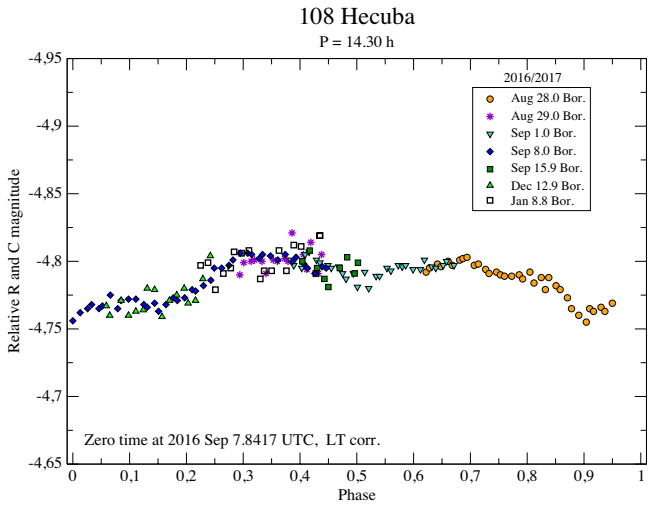


Fig. E.2: Composite light curve of (108) Hecuba from the years 2016-2017.

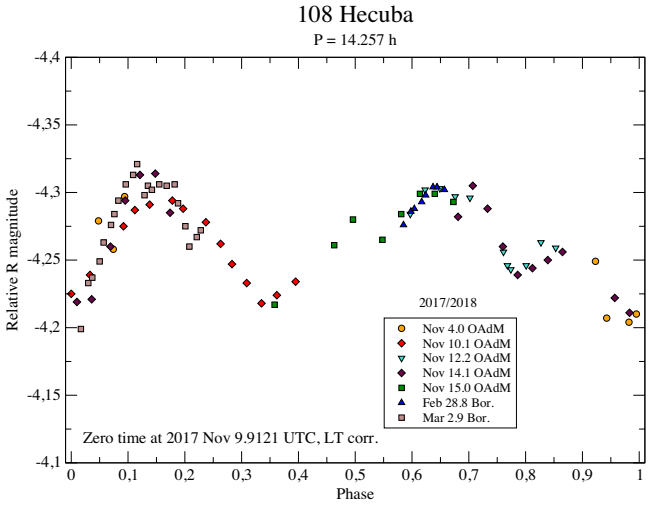


Fig. E.3: Composite light curve of (108) Hecuba from the years 2017-2018.

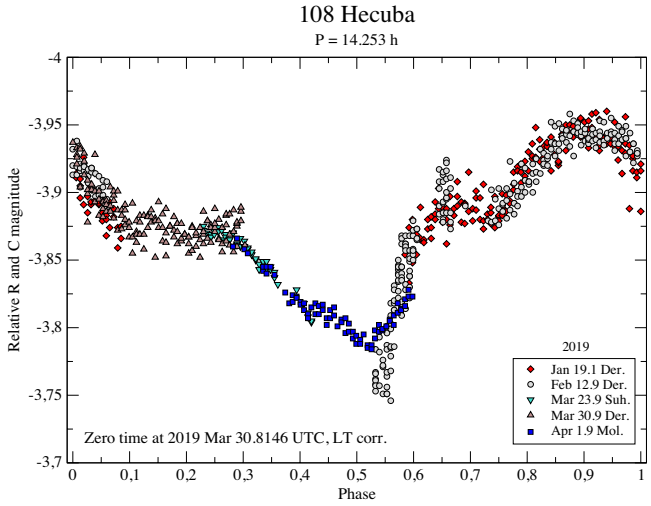


Fig. E.4: Composite light curve of (108) Hecuba from the year 2019.

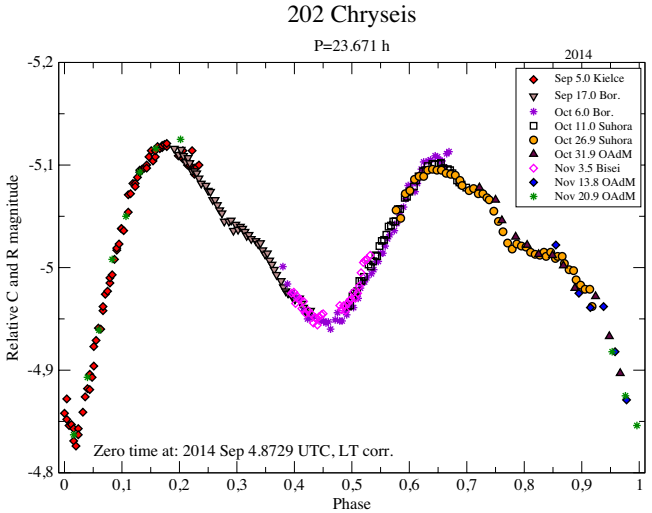


Fig. E.5: Composite light curve of (202) Chryseis from the year 2014.

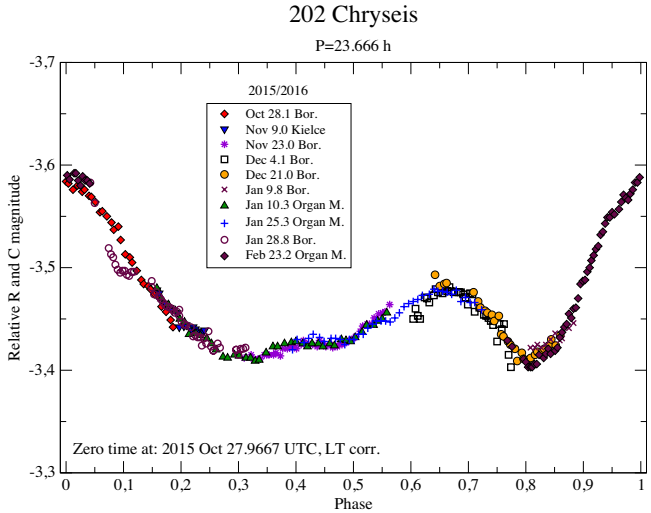


Fig. E.6: Composite light curve of (202) Chryseis from the years 2015-2016.

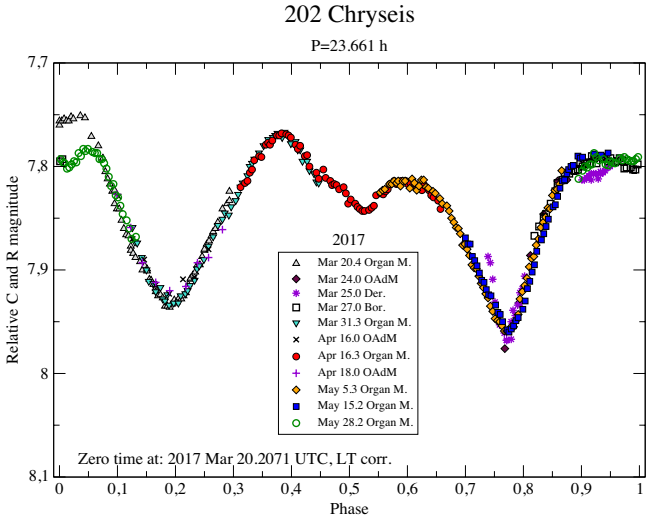


Fig. E.7: Composite light curve of (202) Chryseis from the year 2017.

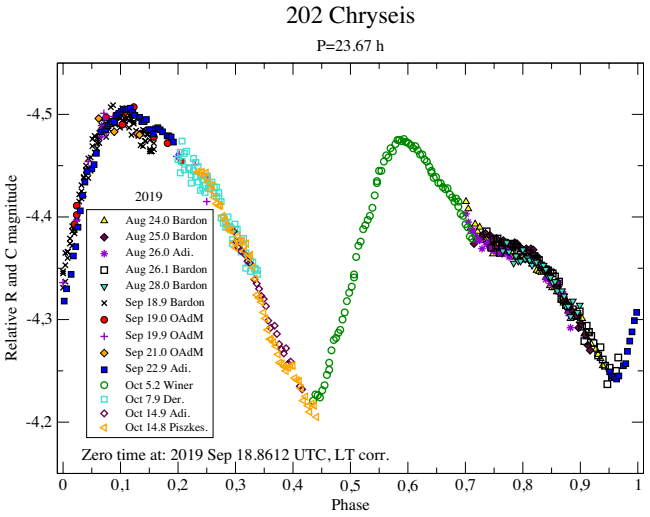


Fig. E.8: Composite light curve of (202) Chryseis from the year 2019.

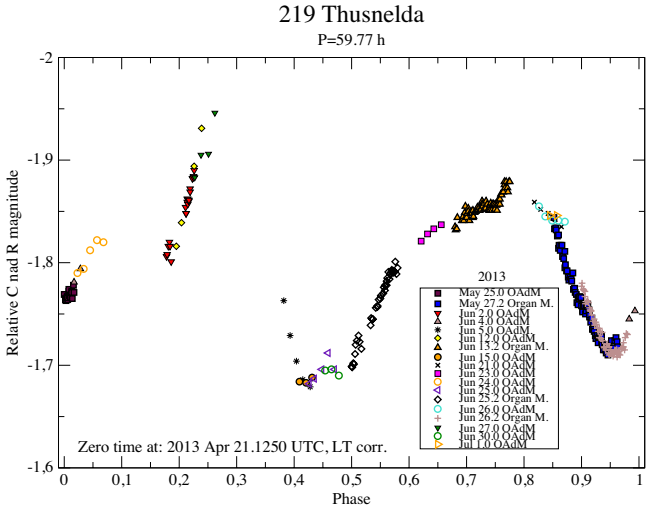


Fig. E.9: Composite light curve of (219) Thusnelda from the year 2013.

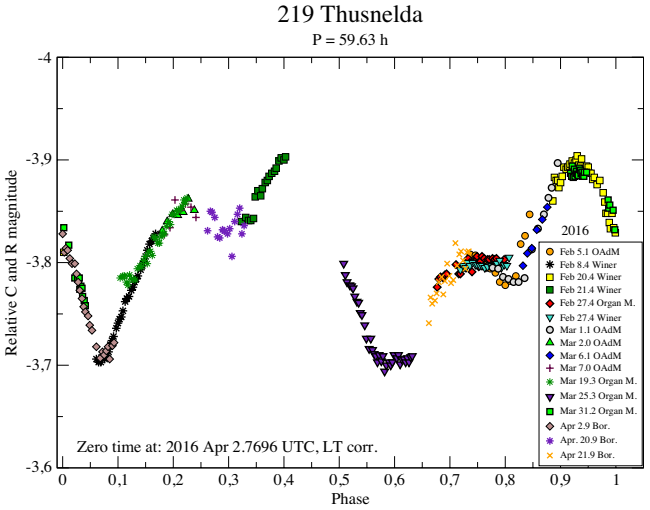


Fig. E.10: Composite light curve of (219) Thusnelda from the year 2016.

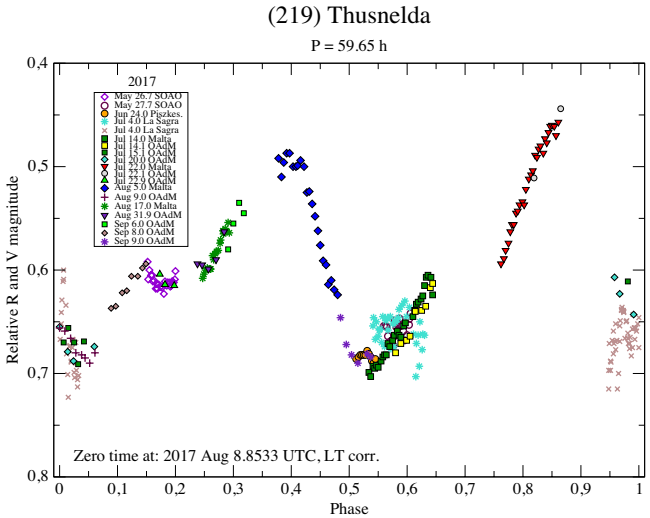


Fig. E.11: Composite light curve of (219) Thusnelda from the year 2017.

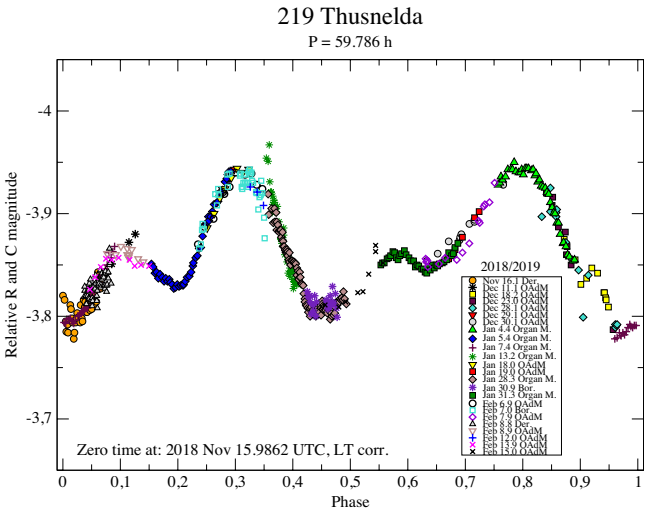


Fig. E.12: Composite light curve of (219) Thusnelda from the years 2018-2019.

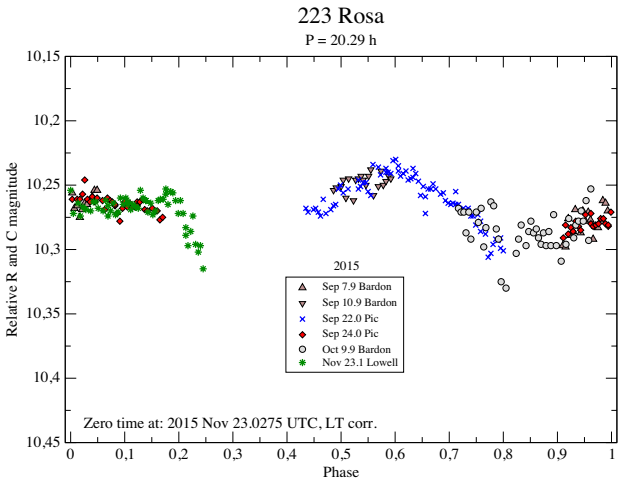


Fig. E.13: Composite light curve of (223) Rosa from the year 2015.

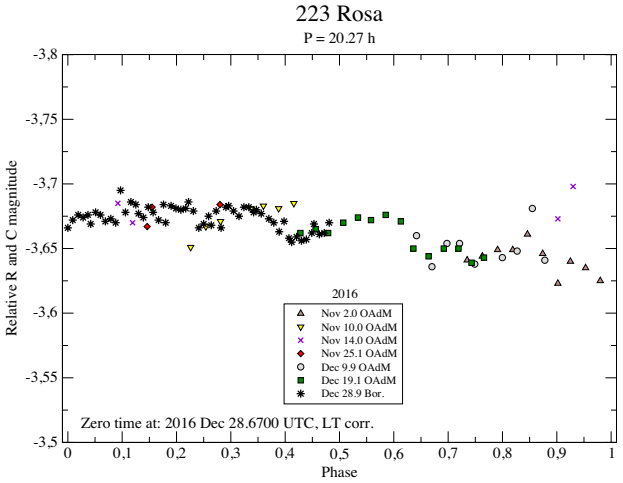


Fig. E.14: Composite light curve of (223) Rosa from the year 2016.

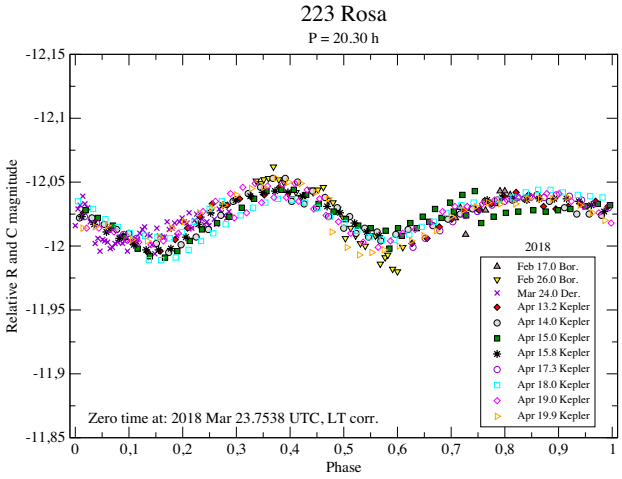


Fig. E.15: Composite light curve of (223) Rosa from the year 2018.

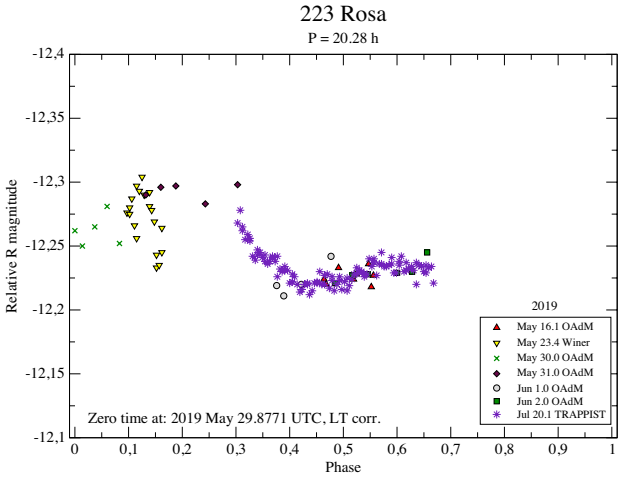


Fig. E.16: Composite light curve of (223) Rosa from the year 2019.

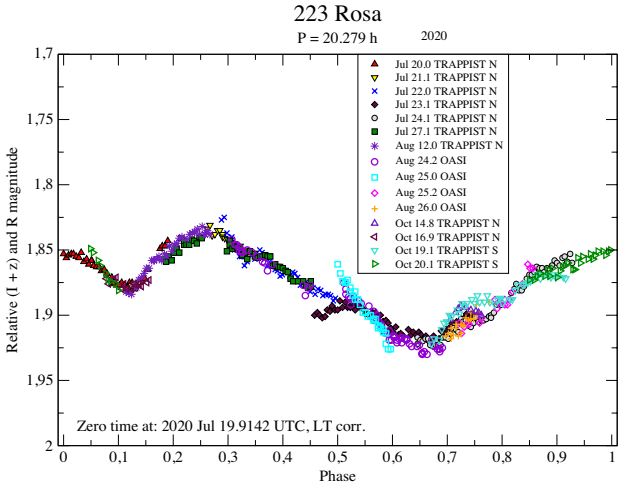


Fig. E.17: Composite light curve of (223) Rosa from the year 2020.

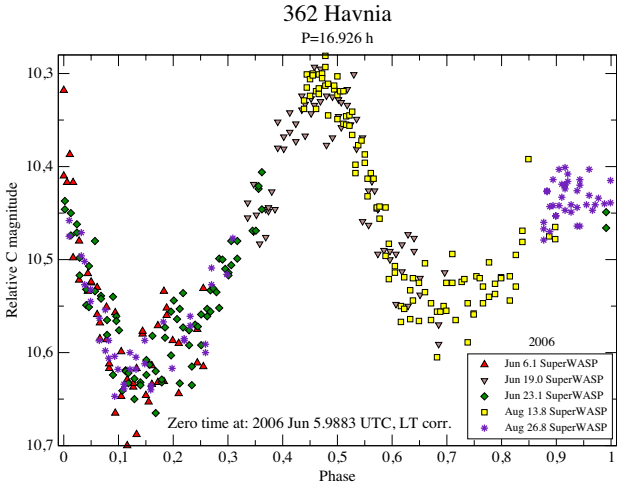


Fig. E.18: Composite light curve of (362) Havnia from the year 2006.

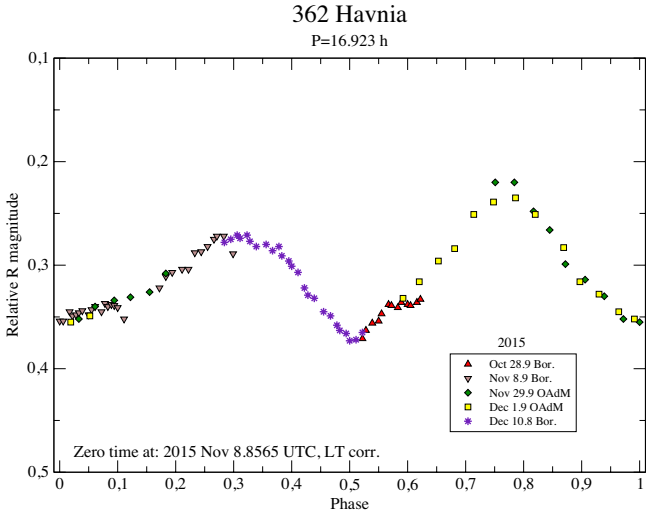


Fig. E.19: Composite light curve of (362) Havnia from the year 2015.

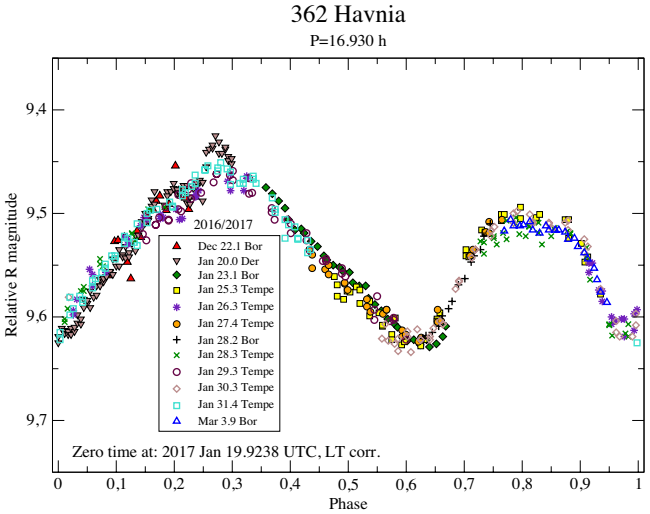


Fig. E.20: Composite light curve of (362) Havnia from the years 2016-2017.

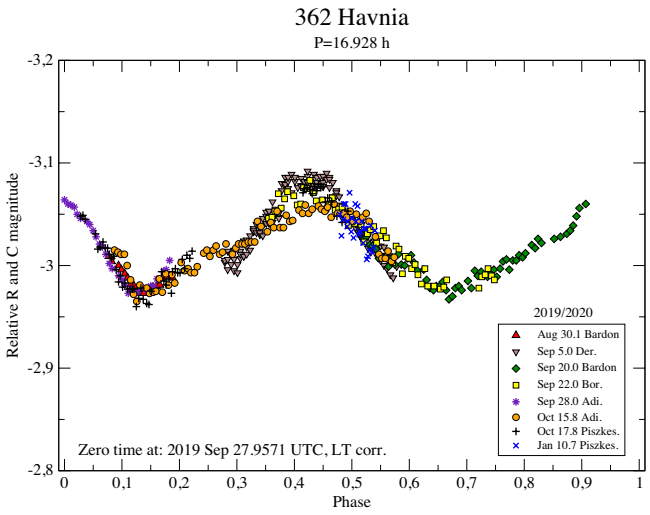


Fig. E.21: Composite light curve of (362) Havnia from the years 2019-2020.

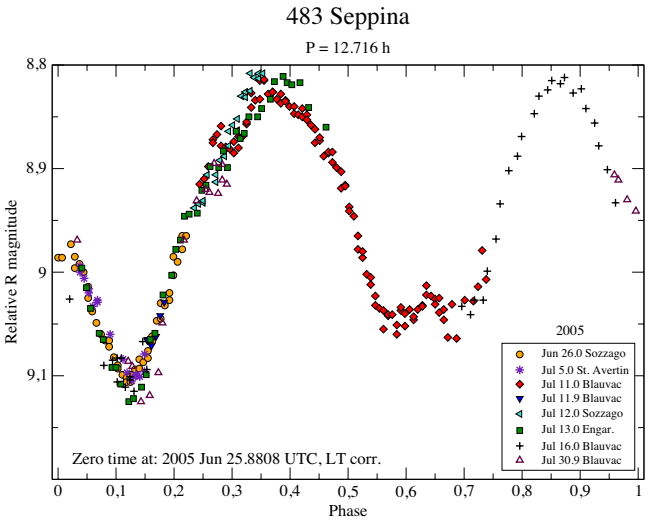


Fig. E.22: Composite light curve of (483) Seppina from the year 2005.

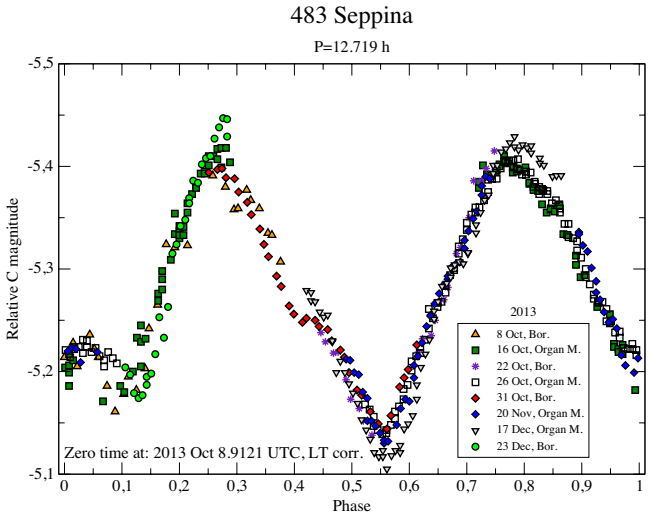


Fig. E.23: Composite light curve of (483) Seppina from the year 2013.

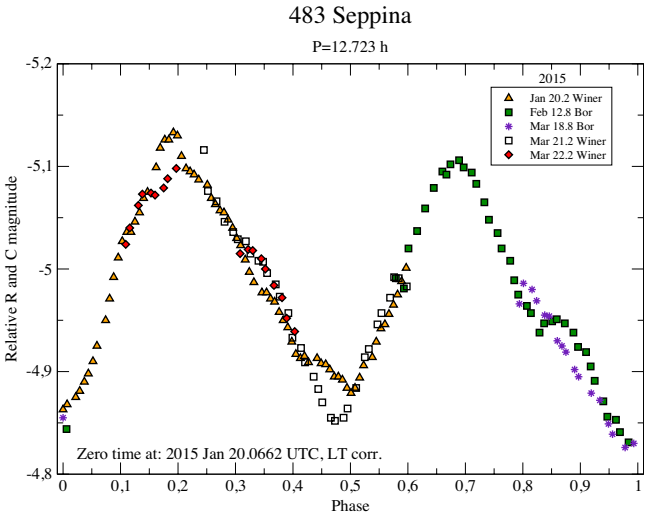


Fig. E.24: Composite light curve of (483) Seppina from the year 2015.

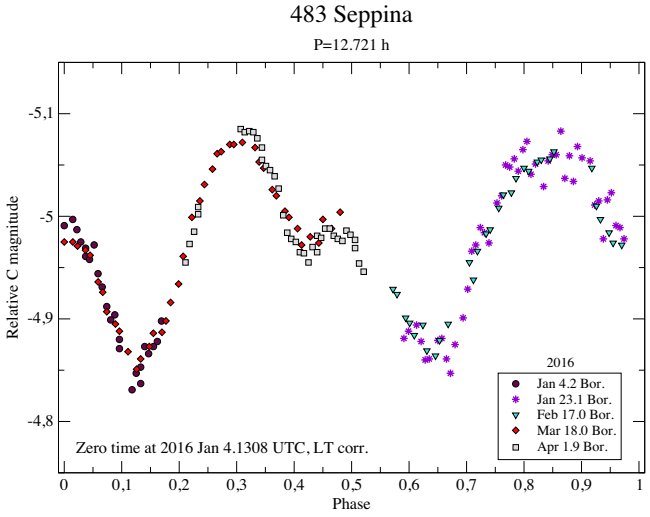


Fig. E.25: Composite light curve of (483) Seppina from the year 2016.

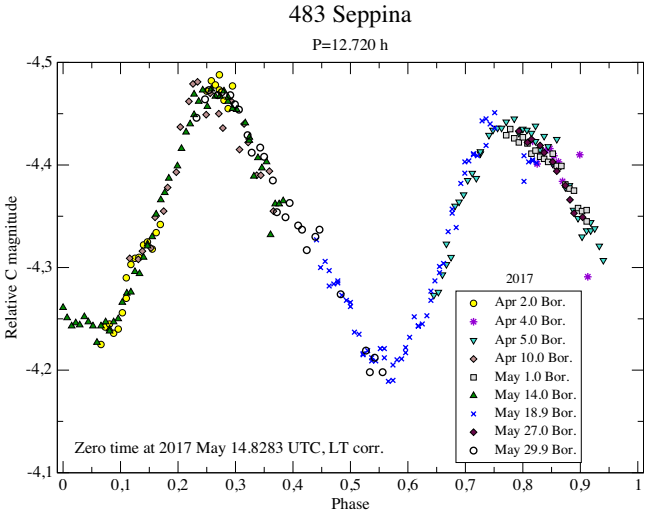


Fig. E.26: Composite light curve of (483) Seppina from the year 2017.

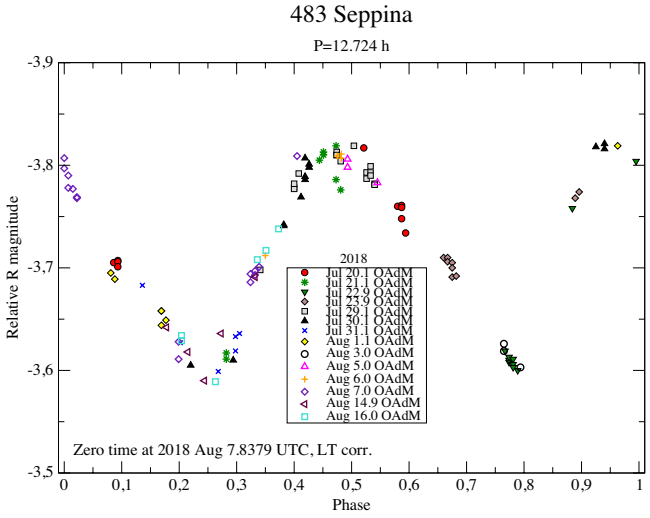


Fig. E.27: Composite light curve of (483) Seppina from the year 2018.

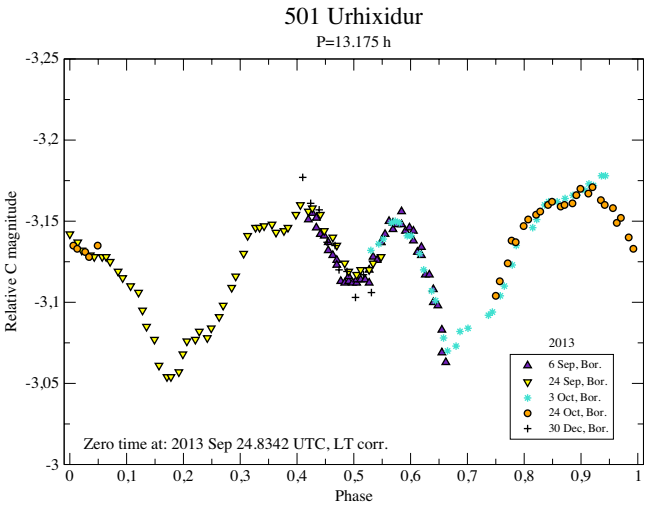


Fig. E.28: Composite light curve of (501) Urhixidur from the year 2013.

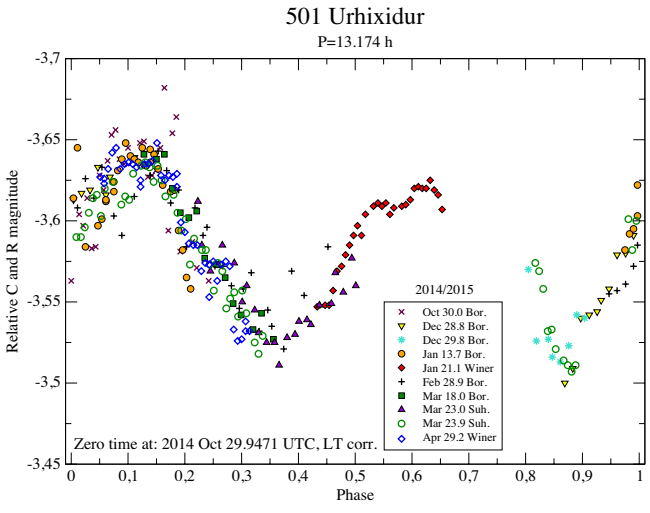


Fig. E.29: Composite light curve of (501) Urhixidur from the years 2014-2015.

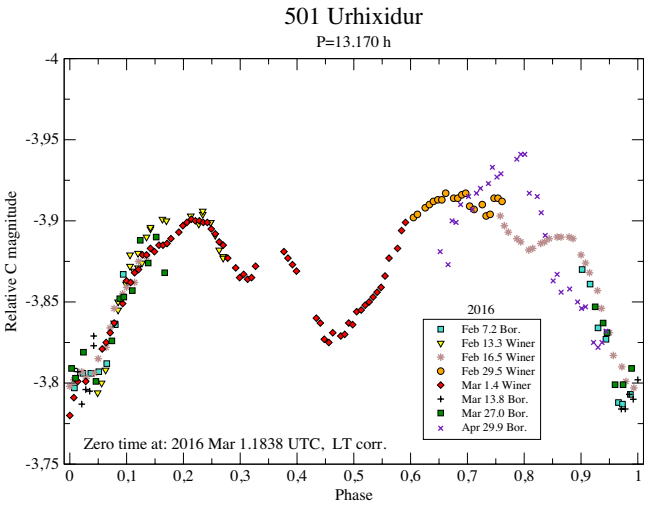


Fig. E.30: Composite light curve of (501) Urhixidur from the year 2016.

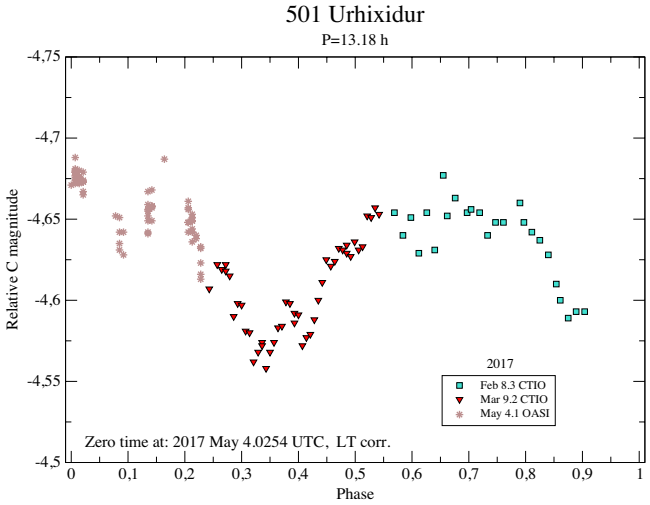


Fig. E.31: Composite light curve of (501) Urhixidur from the year 2017.

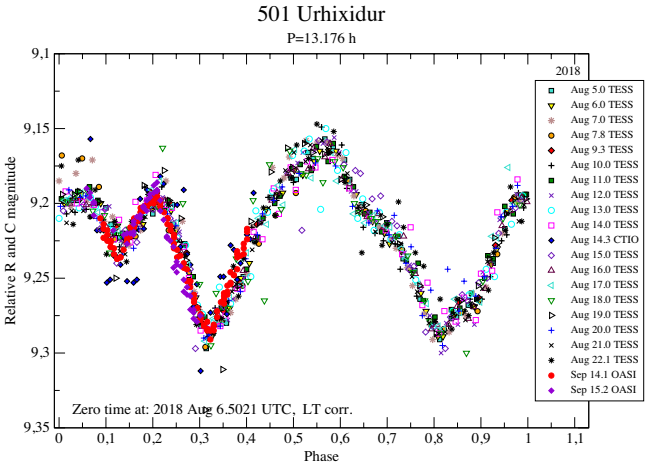


Fig. E.32: Composite light curve of (501) Urhixidur from the year 2018.

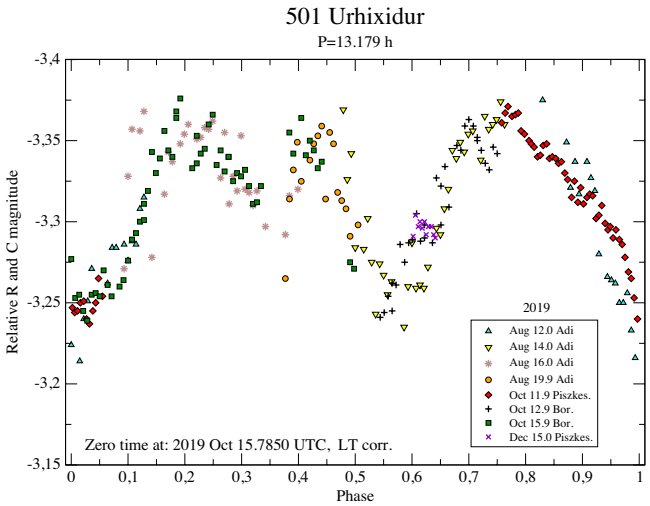


Fig. E.33: Composite light curve of (501) Urhixidur from the year 2019.

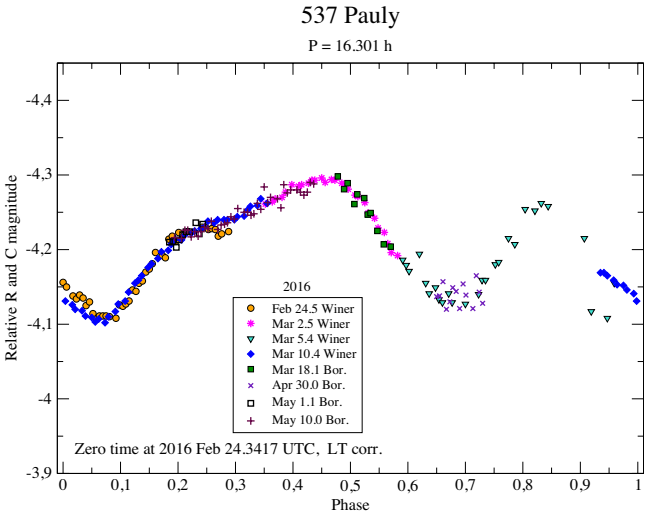


Fig. E.34: Composite light curve of (537) Pauly from the years 2016.

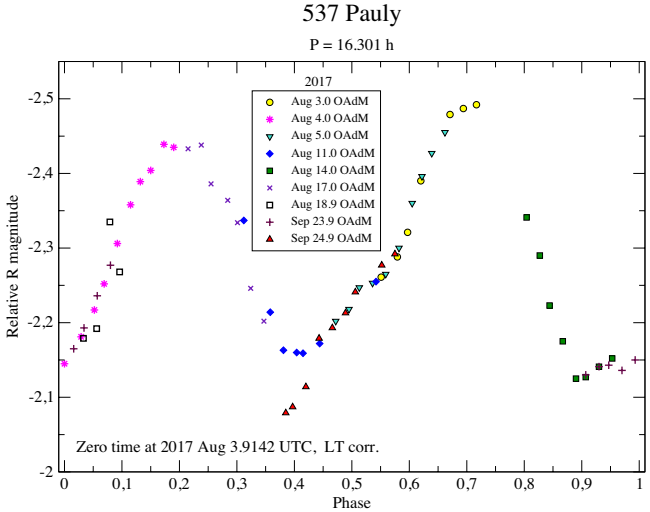


Fig. E.35: Composite light curve of (537) Pauly from the years 2017.

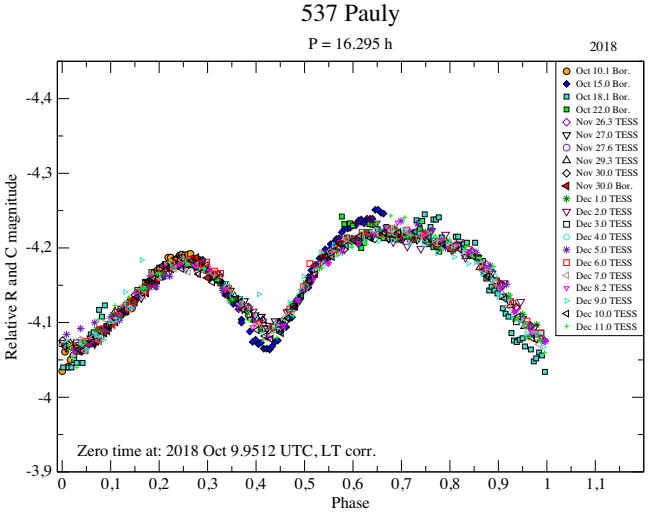


Fig. E.36: Composite light curve of (537) Pauly from the year 2018.

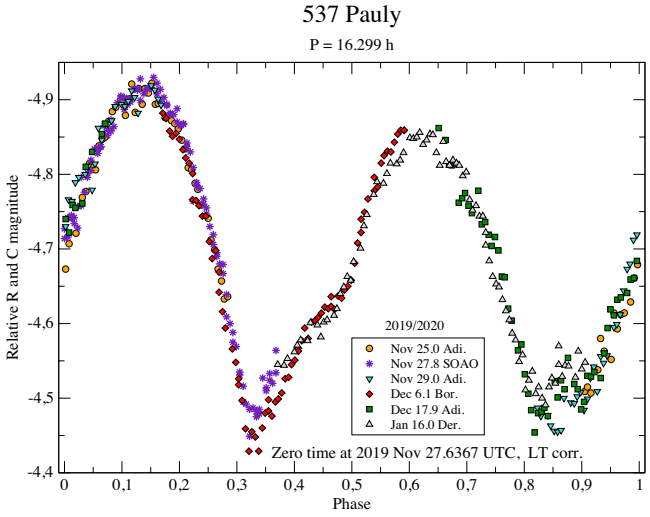


Fig. E.37: Composite light curve of (537) Pauly from the years 2019-2020.

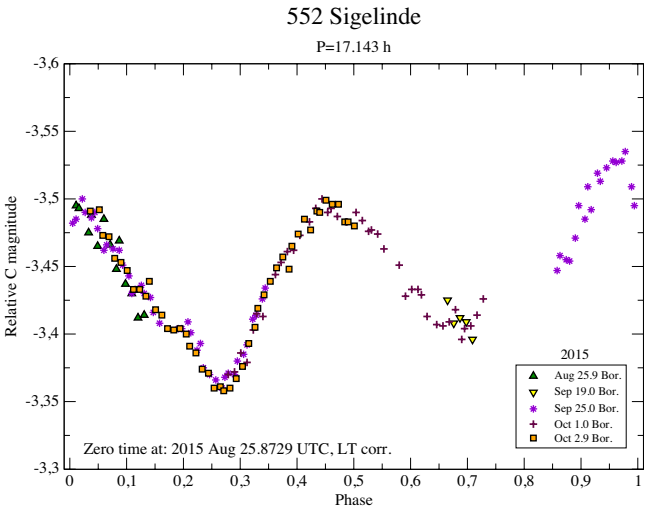


Fig. E.38: Composite light curve of (552) Sigelinde from the year 2015.

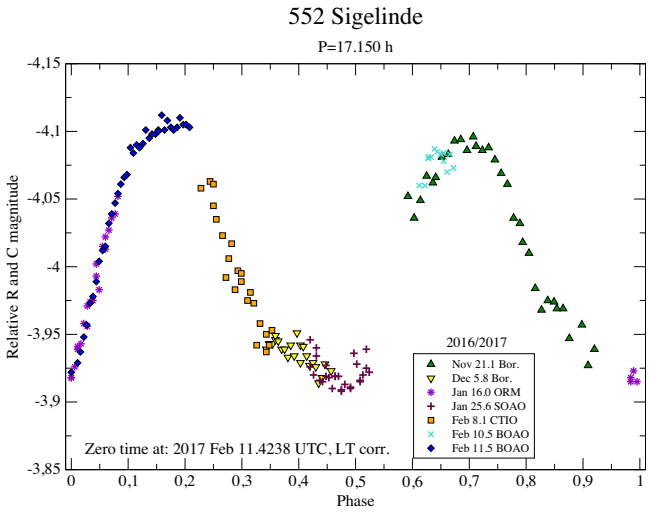


Fig. E.39: Composite light curve of (552) Sigelinde from the years 2016-2017.

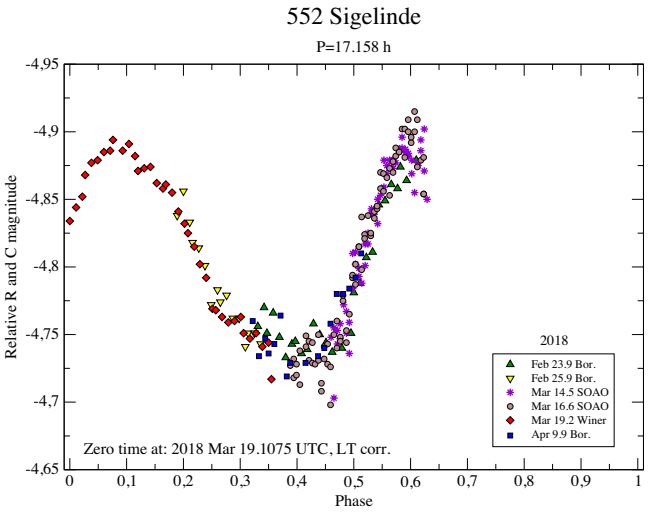


Fig. E.40: Composite light curve of (552) Sigelinde from the year 2018.

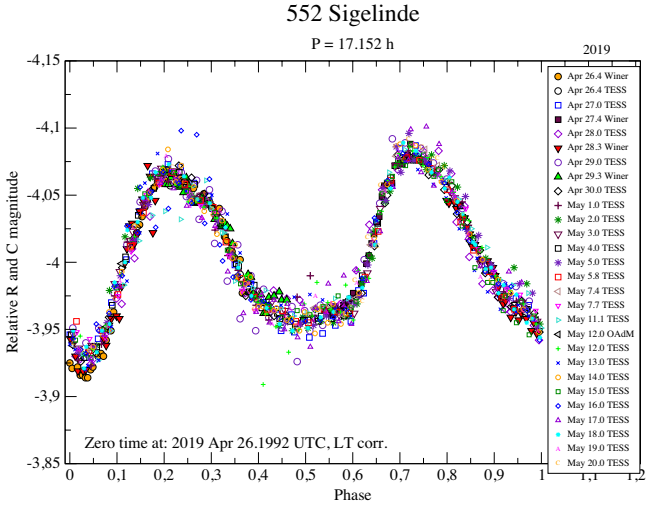


Fig. E.41: Composite light curve of (552) Sigelinde from the year 2019.

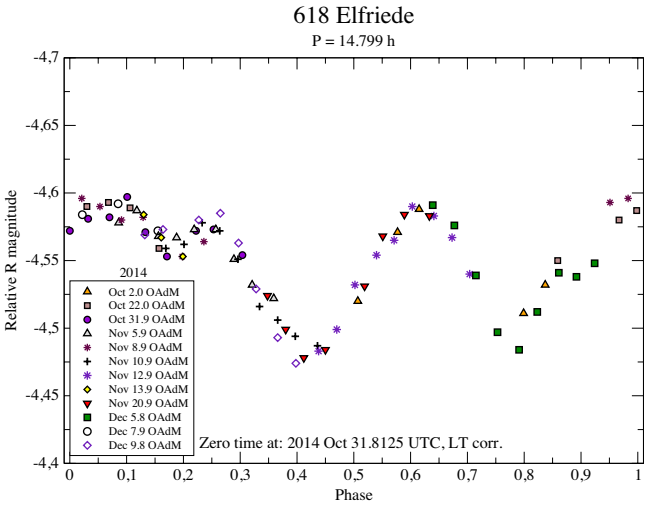


Fig. E.42: Composite light curve of (618) Elfriede from the year 2014.

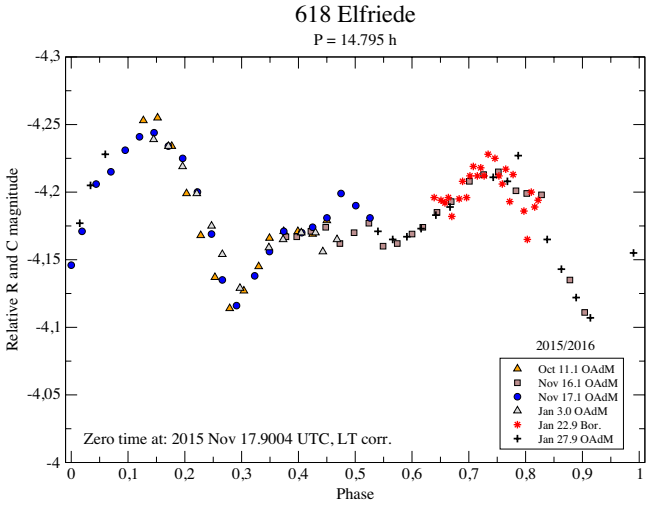


Fig. E.43: Composite light curve of (618) Elfriede from the years 2015-2016.

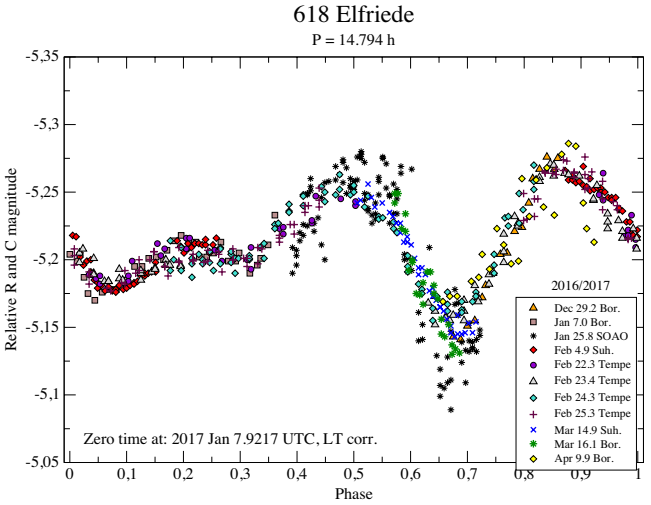


Fig. E.44: Composite light curve of (618) Elfriede from the year 2017.

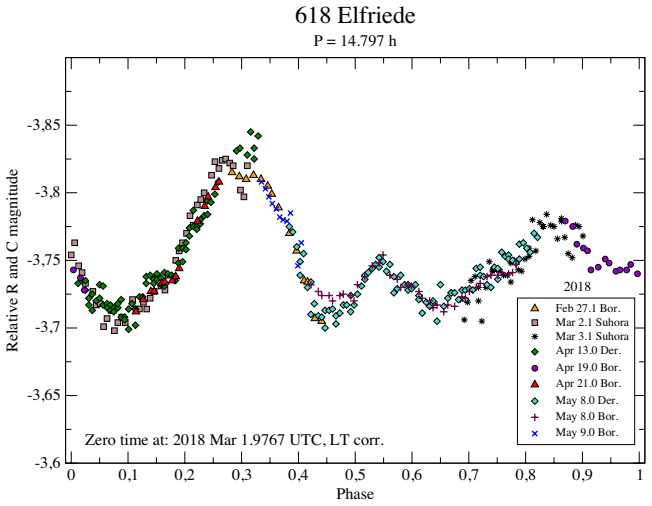


Fig. E.45: Composite light curve of (618) Elfriede from the year 2018.

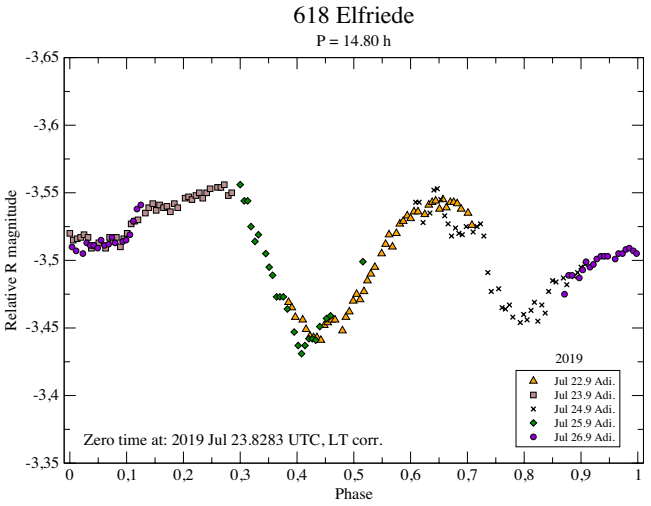


Fig. E.46: Composite light curve of (618) Elfriede from the year 2019.

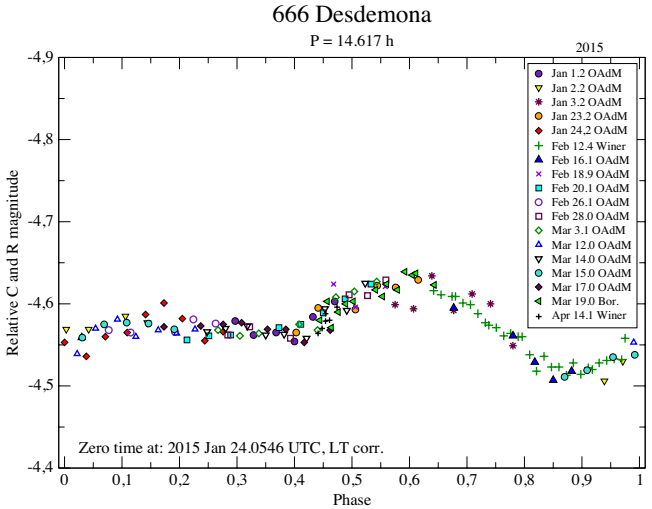


Fig. E.47: Composite light curve of (666) Desdemona from the year 2015.

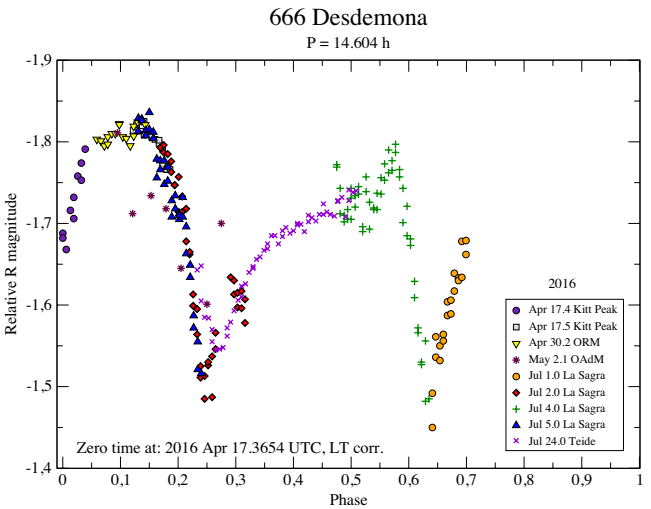


Fig. E.48: Composite light curve of (666) Desdemona from the year 2016.

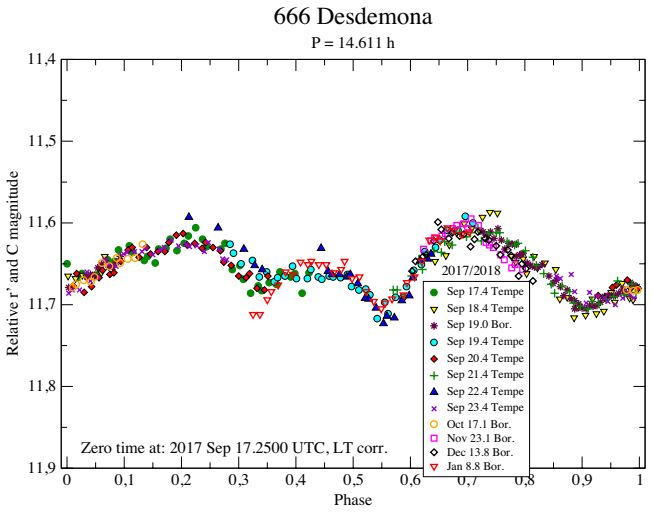


Fig. E.49: Composite light curve of (666) Desdemona from the years 2017-2018.

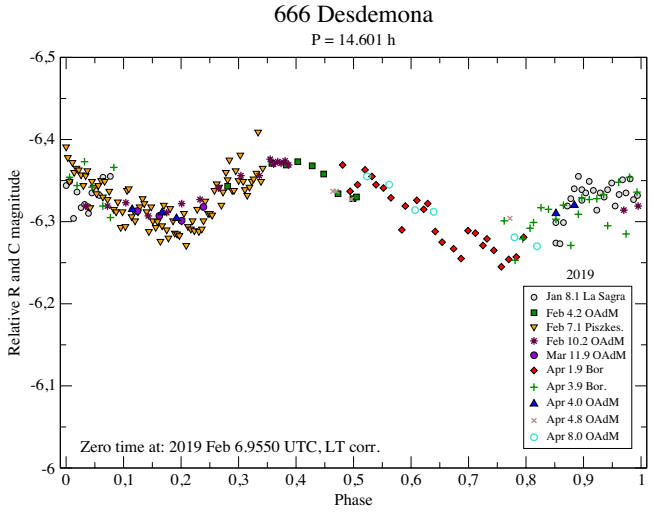


Fig. E.50: Composite light curve of (666) Desdemona from the year 2019.

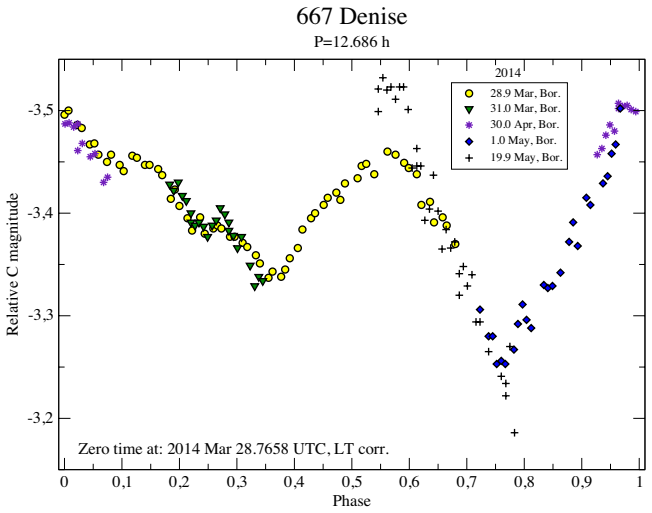


Fig. E.51: Composite light curve of (667) Denise from the year 2014.

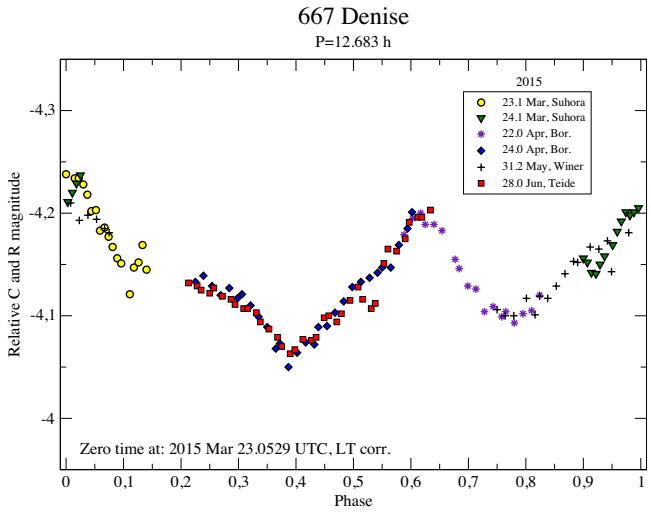


Fig. E.52: Composite light curve of (667) Denise from the year 2015.

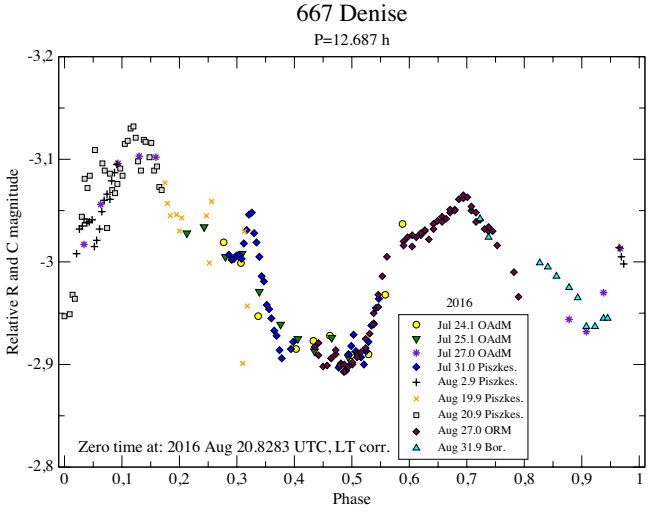


Fig. E.53: Composite light curve of (667) Denise from the year 2016.

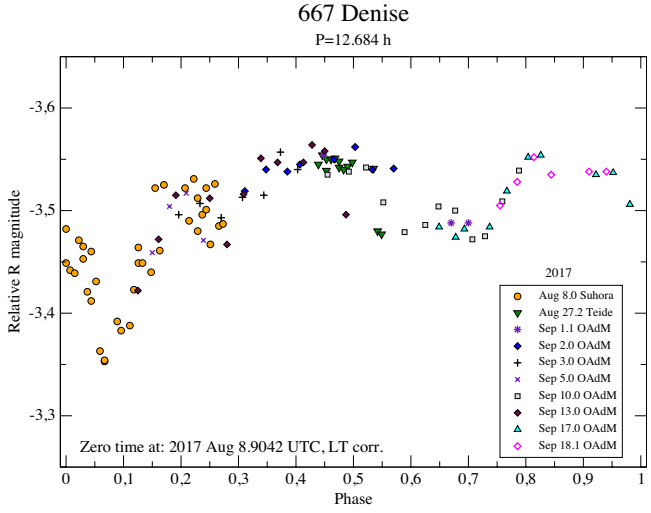


Fig. E.54: Composite light curve of (667) Denise from the year 2017.

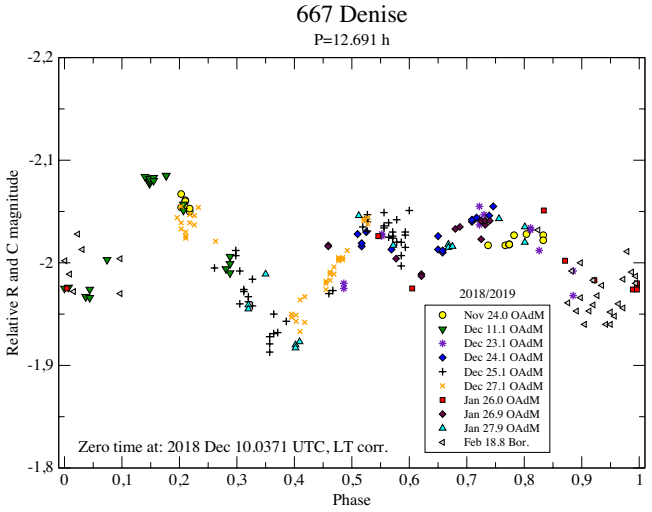


Fig. E.55: Composite light curve of (667) Denise from the years 2018-2019.

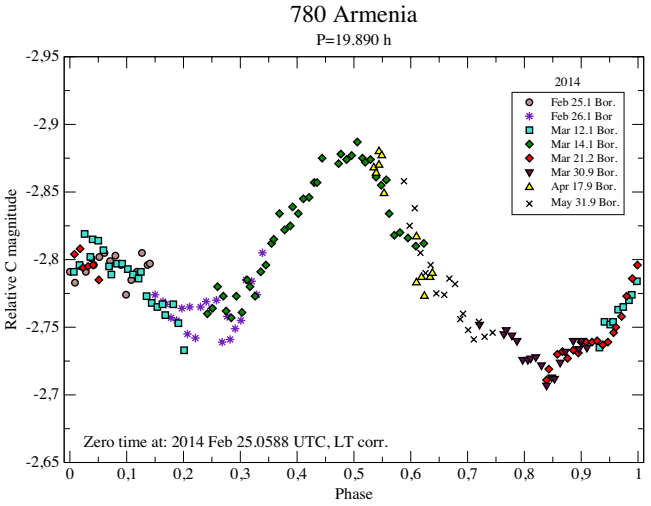


Fig. E.56: Composite light curve of (780) Armenia from the year 2014.

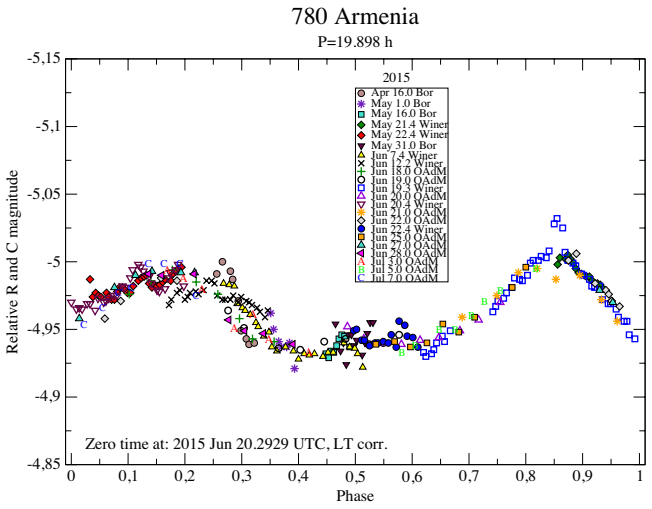


Fig. E.57: Composite light curve of (780) Armenia from the year 2015.

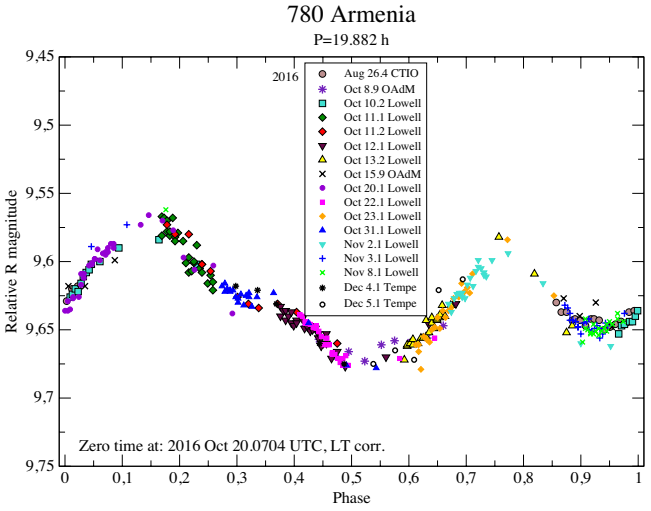


Fig. E.58: Composite light curve of (780) Armenia from the year 2016.

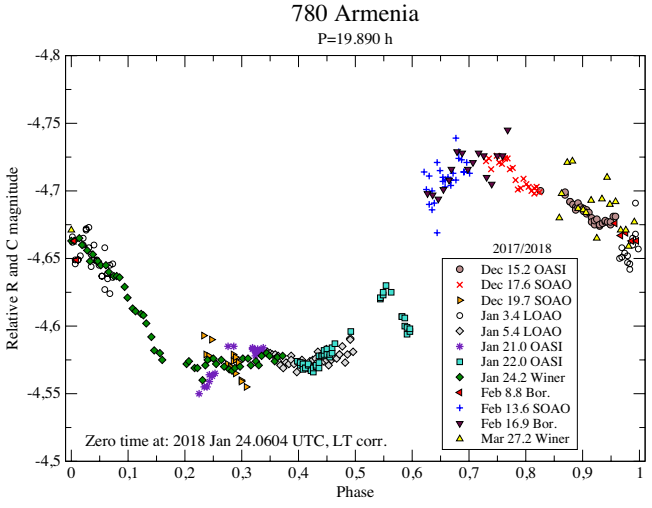


Fig. E.59: Composite light curve of (780) Armenia from the years 2017-2018.

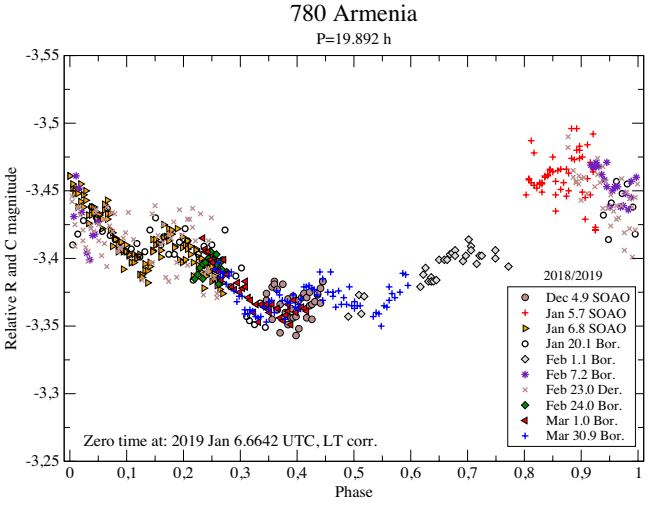


Fig. E.60: Composite light curve of (780) Armenia from the years 2018-2019.

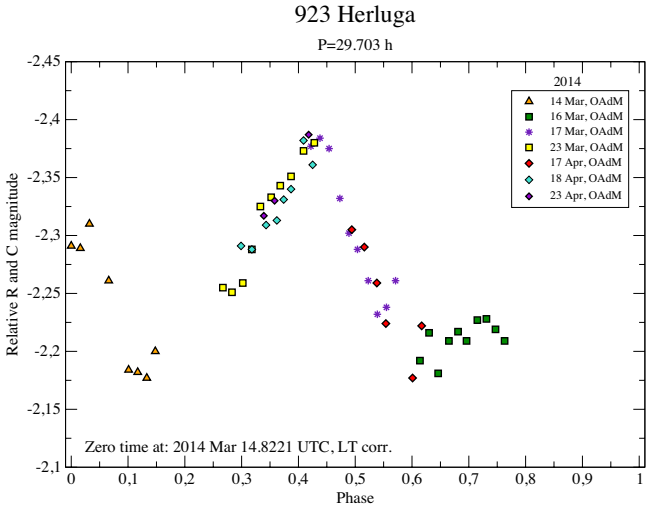


Fig. E.61: Composite light curve of (923) Herluga from the year 2014.

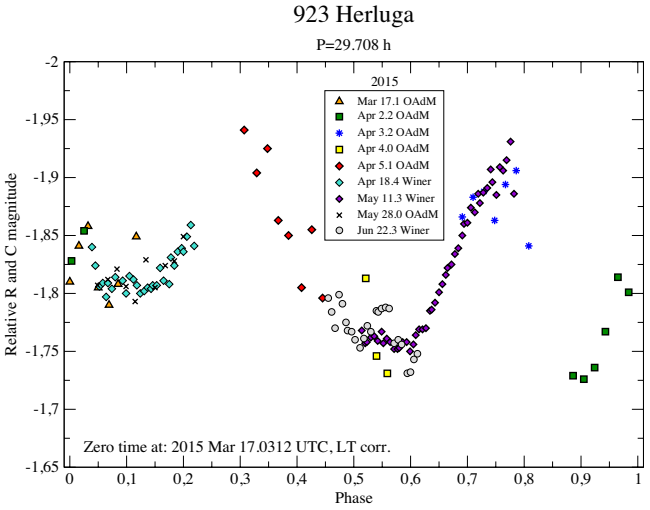


Fig. E.62: Composite light curve of (923) Herluga from the year 2015.

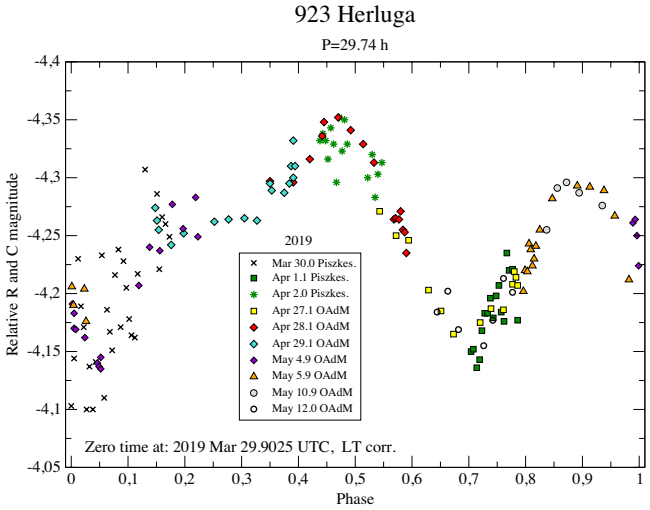


Fig. E.63: Composite light curve of (923) Herluga from the year 2019.

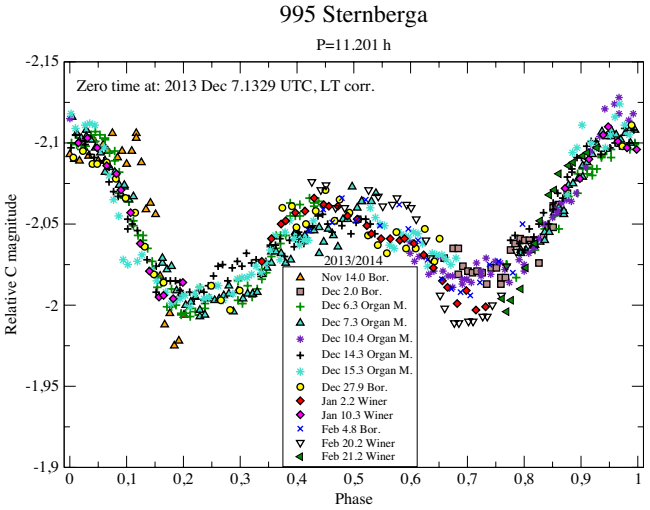


Fig. E.64: Composite light curve of (995) Sternberga from the years 2013-2014.

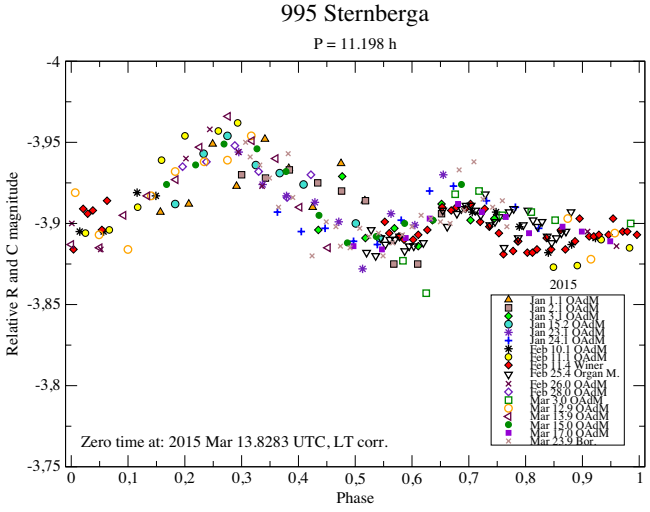


Fig. E.65: Composite light curve of (995) Sternberga from the year 2015.

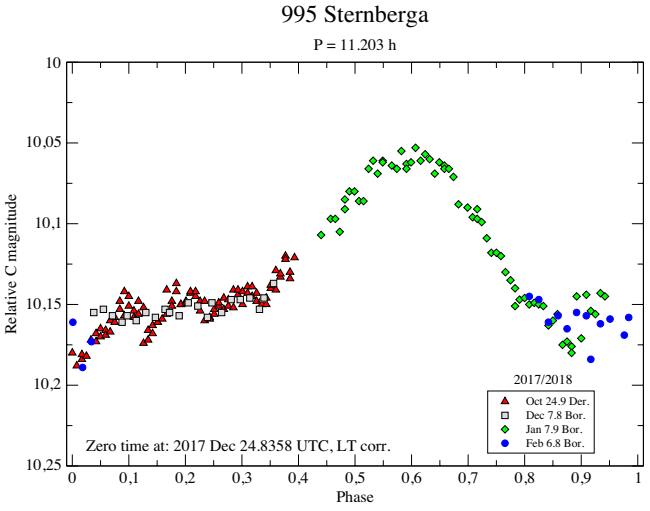


Fig. E.66: Composite light curve of (995) Sternberga from the years 2017-2018.